Journal of Building Engineering 55 (2022) 104681

Contents lists available at ScienceDirect

Journal of Building Engineering

journal homepage: www.elsevier.com/locate/jobe

Assessing the impact of urban microclimate on building energy demand by coupling CFD and building performance simulation

J. Brozovsky [a,*], J. Radivojevic [b], A. Simonsen [c]

[a] Department of Architecture and Technology, Faculty for Architecture and Design, NTNU – Norwegian University of Science and Technology, Høgskoleringen 1, 7491, Trondheim, Norway
[b] Spesialfag Bygg, Rambøll Norge AS, Postboks 9420 Torgarden, 7493, Trondheim, Norway
[c] Process Technology, SINTEF Industry, S.P. Andersens Veg 15B, 7031, Trondheim, Norway

ARTICLE INFO

Keywords:
Urban microclimate
Computational fluid dynamics
Building performance simulation
Cold climate
Urban physics
Materials

ABSTRACT

To quantify the effect of different compositions of the urban surface on the urban microclimate, building energy demand, and summerly overheating of a selected 13-floor office high-rise building in Trondheim, Norway, a validated Computational Fluid Dynamics model is coupled with Building Performance Simulation. In total, four scenarios were investigated in three one-week periods in summer (15.06.20–21.06.20), autumn (16.09.20–22.09.20), and winter (21.12.20–27.12.20). The scenarios were: (1) *base case* or current situation; (2) *no vegetation* in the entire domain with no trees and grass surfaces being substituted with concrete; (3) *all vegetation* with all concrete, asphalt, and pavements replaced by grass; and (4) the base case situation with highly improved insulation levels of surrounding buildings. The results demonstrate clear benefits from urban greening during a one-week heat wave as the *no vegetation* scenario increased the cooling energy demand by 28.5%. The positive effect of evapotranspiration from grass surfaces was noticeable especially on the lowest two floors, where cooling energy demands were halved. During the simulated weeks in autumn and winter, the *no vegetation* scenario resulted in respectively 3.5% and 0.9% lower heating energy demands. At the investigated building, improving the insulation properties of all modeled surrounding buildings led to 0.1 °C higher average air temperatures during summer, and 0.1 °C lower during winter, while they remained unchanged in autumn. However, the energy demands were 0.8%, 0.9%, and 0.8% higher compared to the *base case* for summer, autumn, and winter, respectively.

1. Introduction

Climate change, ongoing urbanization, population growth, and their associated environmental consequences are among the major challenges that humanity faces in the 21st century [1,2]. In these challenges, the building and construction sector, as well as cities, hold a central role. Between 67 and 76% of global energy use and 71–76% of carbon dioxide emissions from global final energy use come from urban areas [1]. Accordingly, *Sustainable Cities and Communities* is one of the 17 Sustainable Development Goals proclaimed by the United Nations [3]. The goal is to create and transform cities into climate-resilient, safe, healthy, and livable environments for their citizens. Especially with globally rising temperatures and more frequent occurrences of heat waves [4–6], the adverse effects of urban climate and especially the urban heat island (UHI) effect on human health and energy use in cities have received increased attention

* Corresponding author.
E-mail address: johannes.brozovsky@ntnu.no (J. Brozovsky).

https://doi.org/10.1016/j.jobe.2022.104681
Received 28 February 2022; Received in revised form 17 May 2022; Accepted 17 May 2022
Available online 21 May 2022

Table 1
Overview of selected published articles on the coupling between exterior CFD and BPS.

Authors	Year	Ref.	City (country)[a]	Type of environment	Research focus	Tools used		Exchanged variables[b]	Type[c]
						CFD	BPS		
Bouyer et al.	2011	[60]	Lyon (FR)	Real	Presenting a CFD-thermoradiative coupled simulation tool	*ANSYS Fluent*	*SOLENE*	AT, MRM, CHTC, ST, R-AV, F-SL	C
Yang et al.	2012	[68]	Guangzhou (CN) Frankfurt (DE)	Generic	Quantitative analysis of building energy performance in the urban context	*ENVI-Met*	*EnergyPlus*	AT, ST, WS, GR, TT, SH	B
Allegrini et al.	2013	[81]	Zürich (CH)	Generic	Effect of an urban neighborhood on local microclimatic conditions	*OpenFOAM*	*CitySim*	ST	A
Yi and Feng	2013	[69]	–	Generic	Propose a coupling methodology between BPS and CFD in order to investigate microclimate impact on building performance	*ANSYS Fluent*	*EnergyPlus*	ST, CHTC	C
Allegrini et al.	2015	[82]	Zürich (CH)	Generic	Investigation of urban heat fluxes for different urban morphologies	*OpenFOAM*	*CitySim*	ST	A
Allegrini et al.	2015	[83]	Zürich (CH)	Generic	Effect of different urban morphologies on the urban microclimate	*OpenFOAM*	*CitySim*	ST	A
Gracik et al.	2015	[56]	State College, PA (US)	Real and Generic	Quantification of the influence of the urban neighborhood on the degradation of building cooling system COP	*OpenFOAM*	*EnergyPlus*	ST, CHTC	C
Liu et al.	2015	[70]	Philadelphia, PA (US)	Generic	Local weather data impact on building energy demand	*PHOENICS*	*EnergyPlus*	AT, ST, WS	C
Malys et al.	2015	[61]	Nantes (FR)	Real	Effect of microclimate on winter energy consumption and summer indoor temperatures in insulated and non-insulated buildings	*SOLENE-microclimate (SATURNE)*	*SOLENE*	AT, ST, WS	C
Gros et al.	2016	[62]	La Rochelle (FR)	Real	Comparing two building densities and their impacts on radiation, wind, indoor temperatures, and energy demand	*SOLENE-microclimate (SATURNE)*	*EnviBatE*	ST, WS, R–SW, VF, IAT	B
Morille et al.	2016	[63]	Nantes (FR)	Generic	Impact of urban greenery on building energy consumption in a street canyon	*SOLENE-microclimate (SATURNE)*	*SOLENE*	CHTC	B
Skehorn et al.	2016	[71]	Manchester (GB)	Generic	Impact of UHI and vegetation on cooling energy use	*ENVI-Met*	*IES-VE*	AT, WS, RH	B
Allegrini and Carmeliet	2017	[84]	Zürich (CH)	Generic	Influence of surface temperatures from BPS, urban form, and buoyancy on air temperatures	*OpenFOAM*	*CitySim*	ST	A
Gobakis and Kolokotsa	2017	[72]	Chania (GR)	Real	Coupling CFD and BPS to improve accuracy for energy performance calculations	*ENVI-Met*	*ESP-r*	AT, WS, WD, R–SW, RH	B
Huang and Li	2017	[73]	Taipei (TW)	Generic	Impact of street canyon topology on a building's peak cooling energy demand	*ENVI-Met*	*EnergyPlus*	AT, WS, WD, RH	B
Merlier et al.	2017	[64]	Lyon (FR)	Generic	Microclimatic effects on the building energy behavior	*SOLENE-microclimate (SATURNE)*	*BuildSysPro*	AT, R–SW, R-LW, AP	B
Allegrini and Carmeliet	2018	[85]	Zürich (CH)	Real	Effect of new buildings on the local microclimate	*OpenFOAM*	*CitySim*	ST	A
Toparlar et al.	2018	[80]	Antwerp (BE)	Real	Impact of urban microclimate and cooling energy demand	*ANSYS Fluent*	*EnergyPlus*	AT, WS, WD	B
Zhang et al.	2018	[65]	Los Angeles, CA (US)	Generic	Coupling CFD and BES tools to enhance the modeling of CHTCs in urban neighborhoods	*ANSYS Fluent*	*EnergyPlus*	ST, CHTC	C
Javanroodi and Nik	2019	[74]	Stockholm (SE)	Generic	Impact of microclimate in typical and extreme climate conditions on the energy performance of an office building	*AutodeskCFD*	*EnergyPlus*	AT, WS, AP, RH	B
Liu et al.	2019	[75]	College Park, MD (US)	Real	Microclimate impact on energy consumption of an academic building	*OpenFOAM*	*EnergyPlus*	AT, WS	B
Natanian et al.	2019	[76]	Tel Aviv (IL)	Generic	Interrelation between form, energy, and urban microclimatic conditions	*ENVI-Met*	*Honeybee (EnergyPlus)*	AT, RH	B
Shirzadi et al.	2019	[77]	Rasht (IR)	Generic	Framework development for improving BPS with urban microclimate interaction	*ANSYS CFX*	*EnergyPlus*	Cp, CHTC, WS	B
Chen et al.	2020	[88]	Guangzhou (CN)	Generic		-	*CitySim*	ST	A

(*continued on next page*)

Table 1 (*continued*)

Authors	Year	Ref.	City (country)[a]	Type of environment	Research focus	Tools used		Exchanged variables[b]	Type[c]
						CFD	BPS		
					Comparison of urban airflow between a solar-induced thermal wall and uniform wall temperature BCs				
Mosteiro-Romero et al.	2020	[78]	Zürich (CH)	Real	Quantitative analysis of building energy demand at district scale considering local microclimatic conditions	*ENVI-Met*	*City Energy Analyst*	AT, WS, RH	B
Shen and Wang	2020	[79]	Chicago, IL (US)	Generic	Influence of neighborhood form on building energy use in winter design conditions	*ANSYS Fluent*	*EnergyPlus*	CHTC, ST	C
Aghamolaei et al.	2021	[89]	Tehran (IR)	Generic	Novel framework to couple radiative and convective fluxes in outdoor environments using CFD and BPS	*ANSYS Fluent*	*EnergyPlus*	ST, RHF	A
Hadavi and Pasdarshahri	2021	[86]	Tehran (IR)	Real	Thermal and aerodynamic effects of urban buildings on microclimate and cooling system performance	*OpenFOAM*	*EnergyPlus*	ST	A
Hadavi and Pasdarshahri	2021	[57]	Tehran (IR)	Real and Generic	Propose a coupling algorithm between CFD and BPS for the accurate simulation of near-building microclimate	*OpenFOAM*	*EnergyPlus*	ST	A
Wong et al.	2021	[87]	Singapore (SG)	Real	Method of distributing BCs from meso- to microscale	*OpenFOAM*	*EnergyPlus*	ST, CHTC, F-HVAC	C
Zhang and Mirzaei	2021	[66]	Los Angeles, CA (US)	Generic	Novel framework for the integration of high-resolution CFD into a coupled model of low-resolution CFD with BPS	*ANSYS CFX* *ANSYS Fluent*	*EnergyPlus*	ST, CHTC	C
Zhang and Mirzaei	2021	[67]	Los Angeles, CA (US)	Generic	Novel framework of virtual dynamic BES-CFD-artificial intelligence coupling	*ANSYS Fluent*	*EnergyPlus*	CHTC	C
This study	–	–	Trondheim (NO)	Real	Influence of different microclimate scenarios on energy use in buildings during different seasons	*ANSYS Fluent*	*IDA ICE*	AT, WS, WD, Cp	B

Abbreviations: Absorbed radiation in vegetation (R-AV), Air pressure (AP), Air temperature (AT), Boundary condition (BC), Building Performance Simulation (BPS), Coefficient of Performance (COP), Computational Fluid Dynamics (CFD), Convective Heat Transfer Coefficient (CHTC), Ground reflectance (GR), Heating Ventilation and Air Conditioning (HVAC), Heat flux from HVAC equipment (F-HVAC), Indoor air temperature (IAT), Latent soil heat flux (F-SL), Longwave radiation (R-LW), Mass rate of moisture (MRM), Pressure coefficient (Cp), Radiative heat flux (RHF), Relative humidity (RH), Shortwave radiation (R–SW), Specific humidity (SH), Surface temperature (ST), Tree transmittance (TT), Wind direction (WD), Wind speed (WS), View factor (VF)

[a] Location of the (real) urban area or climate data

[b] Variables generated in one software environment and used as input in the other

[c] Type A: BPS provides BCs for CFD, Type B: CFD provides BCs for BPS, Type C: CFD and BPS provide BCs to each other (two-way coupling, mostly in an iterative approach)

from researchers, authorities and the general public.

The UHI is defined as the characteristic warmth of a city, often approximated by the temperature difference between a city and its rural surroundings [7]. Adverse effects of the UHI can be for instance thermal discomfort for urban dwellers [8,9], excess mortality [10–12], and increased building cooling demands [12–14]. They were reported not only in warm or temperate but also in cold and polar climate zones [15–17]. Even in Scandinavia, studies illustrated heat wave-related health risks and mortality for the case of Oslo [18] and several municipalities in Sweden [19]. Compared to a share of about 90% in the USA or nearly 60% in China, less than 10% of households in the European Union have air conditioning installed to counteract excessive heat [20]. The share in Scandinavia can be expected to be far lower. On the other hand, the UHI was found to contribute to a net decrease of building energy use through larger heating energy savings than cooling energy increases in the north of the USA [21,22], Russia [23], or in Northeast China [24,25]. Additionally, inner-city climatic conditions were found to shield people from extreme cold stress during winter in the Russian Far East.

Some of the major causes of the UHI phenomenon are for instance the lack of evapotranspiration from vegetation and unsealed surfaces, a high share of heavy materials with a low surface albedo that store significant amounts of energy from incoming short- and long-wave radiation, decreased turbulent heat transport in densely built-up areas, and anthropogenic heat release from buildings, fuel combustion in vehicles, or industrial processes [26,27]. The individual contributing shares of the afore-mentioned causes to the UHI, however, are strongly dependent on the specific characteristics of a city.

Steadily rising computational power and decreasing computational costs have led to the development and increased application of numerical tools to study the urban climate since the early 2000s [28–30]. As opposed to field measurements, numerical tools can be used to easily investigate different scenarios and provide the climate variables for every location in the investigated area instead of only a few measurement points. The typical scale to study outdoor thermal comfort or the impact of the urban climate on building energy use is the meteorological microscale (horizontal extension between 2 m and 2 km) [31]. The local climatic conditions in this scale are usually referred to as *microclimate*.

In the literature, Computational Fluid Dynamics (CFD) has been used in a wide range of numerical studies to investigate the urban microclimate, e.g., pedestrian wind comfort [32–36], pollutant dispersal [37–40], wind-driven rain [41–43], or outdoor thermal comfort [44–46]. However, its application often comes along with oversimplification due to high computational efforts. The consequences of such oversimplifications and other challenges related to the application of CFD to simulate the urban microclimate are discussed in Ref. [47].

A powerful way to investigate the impact of urban microclimate on building energy use is to couple CFD with building performance simulation (BPS). This can be done either to supply the CFD side with more detailed boundary conditions (BC) from BPS-output (type A), to use CFD-generated data as BC in BPS software (type B), or both (type C). While types A and B are one-way coupling techniques which means that data is exchanged only in one direction, type C is a two-way coupling approach. The advantage of two-way coupling is generally a higher accuracy, as it involves several iterations of data exchange between the models. Consequently, they influence each other's results until acceptable accuracy is reached before moving to the next time step in a dynamic simulation. On the other hand, one-way coupling is computationally less expensive than two-way coupling [48]. Moreover, it can be distinguished between the coupling of BPS with building-interior [49–55] and exterior CFD. In Table 1, an overview of selected published scientific articles coupling exterior CFD with BPS is presented. This overview is not exhaustive and only represents a subset of all relevant literature.

From the 32 listed articles (excluding this study) in Table 1, most studies (13 articles, 40.6%) are of one-way coupling type B, i.e., supplying BPS software with BCs from CFD simulations. Ten studies (31.3%) used a two-way coupling approach (type C) and in nine cases (28.1%), BPS results were used for more accurate BCs in CFD (type A). Most commonly, surface temperature (ST) was exchanged between the tools (19 articles, 59.4%), followed by air temperature (AT) in 14 studies (43.8%) and wind speed (WS) in 12 articles (37.5%). A clear majority of 20 articles (62.5%) considered generic urban environments as opposed to ten (31.3%) for real cities. In two articles, both real and generic environments were studied [56,57]. In both cases, the real environment served as a validation case

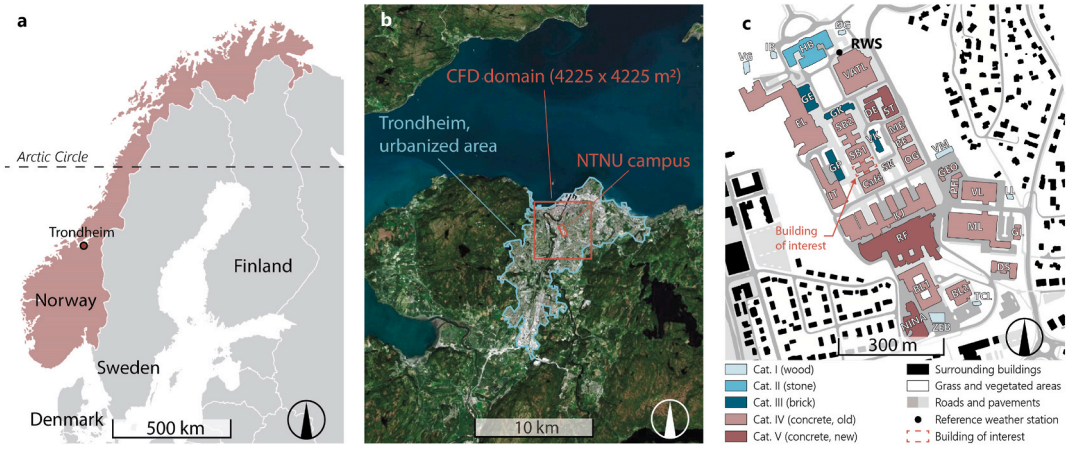

Fig. 1. (a) Location of Trondheim within Norway and Fennoscandia. (b) Satellite image of Trondheim's built-up area (from the Norwegian Mapping Authority, www.kartverket.no). (c) Site plan of the NTNU campus with building categories, surface types, and the highlighted building of interest.

study for the following investigation of a generic urban layout. Half of the studies used weather data from European cities for their analysis with Zürich in Switzerland representing the most-used study location (six times). It is also evident that the open-source tools *OpenFOAM* (http://www.openfoam.org/) and *EnergyPlus* [58] were the most popular among the selected articles in Table 1, as they were used 10 (31.3%) and 18 (56.3%) times, respectively. However, there are many other tools that can be used to simulate the urban microclimate and couple CFD and BPS. Stavrakakis et al. [59] review the most common tools and their capabilities with this regard.

Due to the high computational cost, coupling exterior CFD and BPS is a relatively new approach which is documented by several articles that propose new methodologies, frameworks, or tools. Bouyer et al. [60] for instance, presented a building thermal sub-model for *SOLENE* which they coupled with *ANSYS Fluent* to investigate the influence of microclimate on building energy demand in Lyon, France. *SOLENE* was in the following extended with a CFD code to *SOLENE-Microclimate* and used in several other studies [61–64]. Zhang et al. [65] and Zhang and Mirzaei [66,67] propose different, complex type C frameworks for coupling *ANSYS Fluent* and in one case *ANSYS CFX* with *EnergyPlus*. Most studies addressed the building energy performance [61–80]. Others addressed the impact of the built environment on microclimatic conditions [81–85], the efficiency of cooling systems [56,57,86], or methods to include and distribute BC in CFD [87,88].

From the reviewed articles in Table 1 it can be seen that only very few studies were conducted in cold and high-latitude climate conditions. Furthermore, no studies could be identified that conducted a seasonal comparison of different scenarios of materials and vegetation at the urban surface as most address summerly overheating only. In this article, CFD simulations of the urban microclimate for the *Gløshaugen* campus of the *Norwegian University of Science and Technology* (NTNU) in Trondheim, Norway, are carried out. This is done for different seasons of the year (summer, autumn, and winter) and four different compositions of the urban surface. These include (1) *base case* or current situation; (2) *no vegetation* in the entire domain with grass surfaces being substituted with concrete; (3) *all vegetation* with all concrete, asphalt, and pavements replaced by grass surfaces; and (4) the base case situation but with improved insulation properties of the building envelopes. The resulting microclimatic conditions around a 13-floor office high-rise building on site are captured and used as climate input for BPS simulations in order to quantify their impact on the building's energy use and summerly overheating. The office building is representative of the major part of buildings at the study site and was selected due to its construction type and year. Section 2 of this article presents the study area, local climate conditions, and the CFD-BPS coupling methodology. In sections 3 and 4, the settings and boundary conditions which were used for the CFD and BPS tool, respectively, are presented. Following the results in section 5 and the discussion in section 6 respectively, section 7 concludes this article.

2. Methodology

2.1. Study area and local climate

The area of interest in this study is the NTNU campus (*Gløshaugen*) in Trondheim, Norway. Located in Central Norway and with an urbanized area of about 70.6 km^2 and 208,000 inhabitants [90], the city lies at a latitude of 63.4° N. The investigated part of NTNU's campus is approximately 0.26 km^2 in size and is situated ca. 1.5 km south of the city center at an altitude between 38 and 49 m a.s.l. Trondheim is embedded in complex terrain to the east, west, and south, and borders a fjord to the north. Referring to Stewart and Oke's [91] classification of urban landscape types, called *Local Climate Zone* (LCZ), the city is mainly characterized by a mix of open, low-rise (LCZ 6), and midrise (LCZ 5) built-up areas, as well as park-like areas (LCZ 9/LCZ B). The built-up areas are frequently traversed by patches of forests (LCZ A) and the meandering *Nidelva* river. The city center can be categorized as *dense midrise* (LCZ 2). The campus itself might be categorized as a mixture of *dense midrise* (LCZ 2) and *open midrise* (LCZ 5). Another essential feature of the city is the large water body of the *Trondheim Fjord* to the north of the city center (LCZ G, see Fig. 1). In total, almost 1.6 km^2 of the domain are covered by water which corresponds to 8.6% of the domain's ground surface area.

Furthermore, Fig. 1 shows a map of the NTNU campus with the different building categories and surface materials, and the building of interest in the center of the campus area (the high-rise of *Sentralbygg 1*, SB1). This building is considered to be a representative building of the study area due to its construction type and year. In this study, it will be used to evaluate the impact of different urban microclimates at the campus on building energy demand and summerly overheating.

Trondheim's climate is categorized as *oceanic* (Dfb) by the Köppen-Geiger climate classification system [92], but closely borders continental, subpolar, and subarctic climates [93]. From November to March, moderate snowfall with periods of milder weather patterns and rain is common. Summers are relatively short and mild, winters long and cool. In the period between 1961 and 1990, the annual mean temperature was 4.8 °C in Trondheim, but due to climate change, temperatures have been rising during the last decades. With an annual mean temperature of 5.8 °C, the most recent norm period from 1991 to 2020 was 1.0 °C higher (5.8 °C) than the previous between 1961 and 1990 [94].

Considering their latitudes, Norway's coastal cities experience a rather mild climate. This is caused by the distinct warming effect from the Gulf Stream [95]. However, the solar elevation angles are generally quite low which results in very limited daylight hours

Table 2
Sun elevation angles and daylight hours for different dates in 2020 for Trondheim, Norway.

Date	Max. sun elevation angle	Time of sunrise	Time of sunset	Length of day
20.03. (vernal equinox)	26.7°	06:18	18:34	12.3 h
20.06. (summer solstice)	50.0°	03:02	23:37	20.6 h
22.09. (autumnal equinox)	26.6°	07:02	19:17	12.3 h
21.12. (winter solstice)	3.3°	10:01	14:31	4.5 h

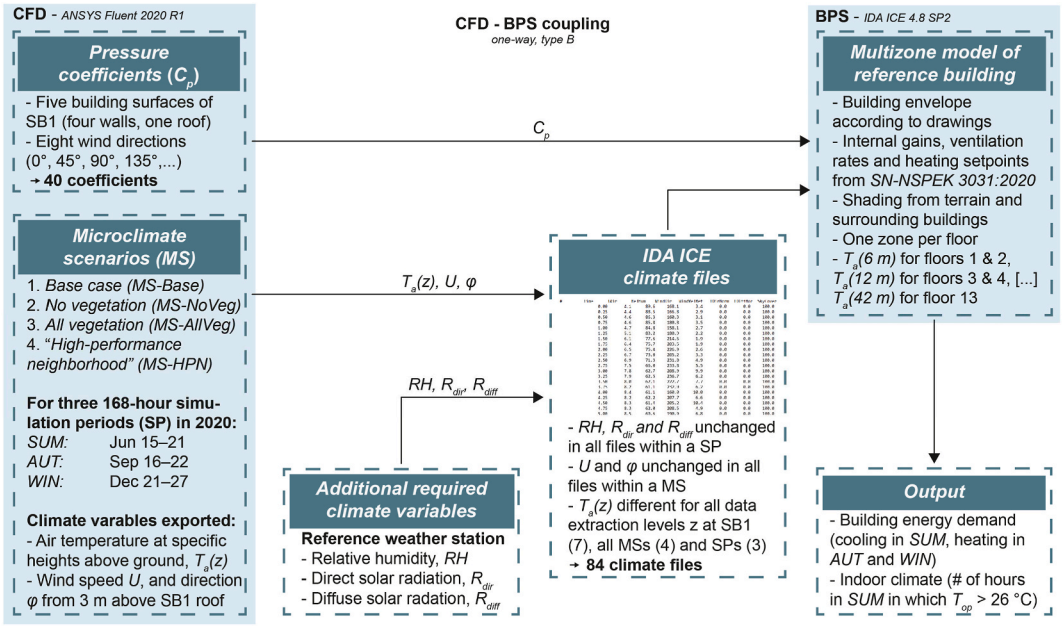

Fig. 2. Coupling methodology between CFD and BPS in this study.

during winter. In summer, on the other hand, the contrary is the case (see Table 2). The low solar altitude during winter in combination with complex, hilly terrain and the urban landscape results in significant shading at the pedestrian level and the lower floors of buildings.

The NTNU Gløshaugen campus features a rather heterogeneous mix of buildings. The oldest dates back to ca. 1850, the newest was finished in 2021, but about half of the gross floor area at the campus was constructed in the 1950s and 1960s (ca. 150,000 m^2). The building heights range from around 6–45 m. While for the smaller buildings, the main construction and façade surface material is wood, the building surfaces of the campus are dominated by heavy materials like stone, brick, and particularly concrete with about 99% of the built gross floor area (GFA).

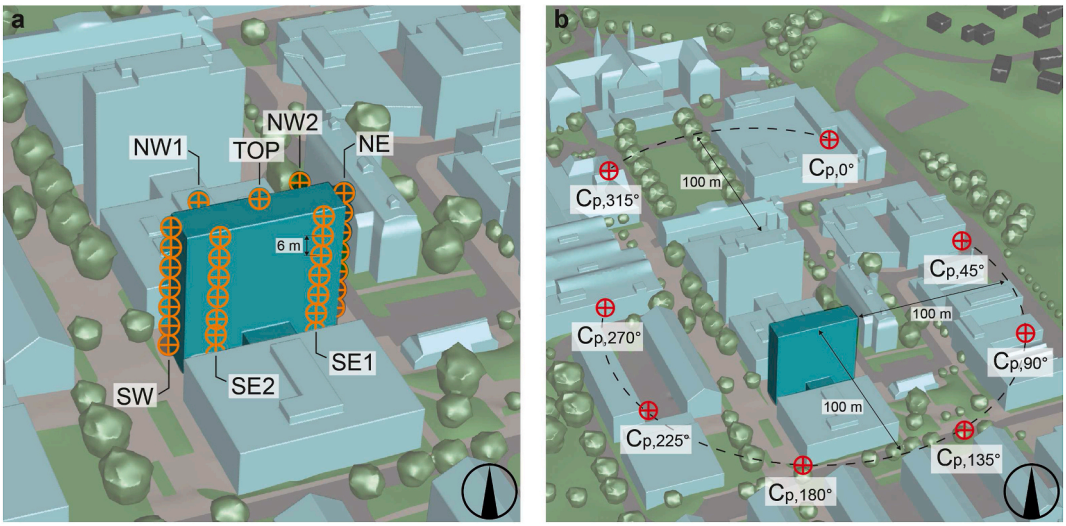

Fig. 3. Location of data logging points in ANSYS Fluent with the building of interest (SB1) highlighted within the central campus area, viewed from the south. (a) shows the temperature logging points (orange markers) with a 2 m horizontal distance from the respective façades and a 6 m vertical spacing between the single points. "TOP" is the data logging point for wind speed and direction, centrally located 3 m above SB1. (b) shows the freestream reference points (red markers) for each wind direction at 100 m distance from SB1. The northern and northwestern reference points are placed at 100 m distance from the neighboring SB2, as this building evokes an upstream wind-blocking effect that disturbs the freestream. (For interpretation of the references to colour in this figure legend, the reader is referred to the Web version of this article.)

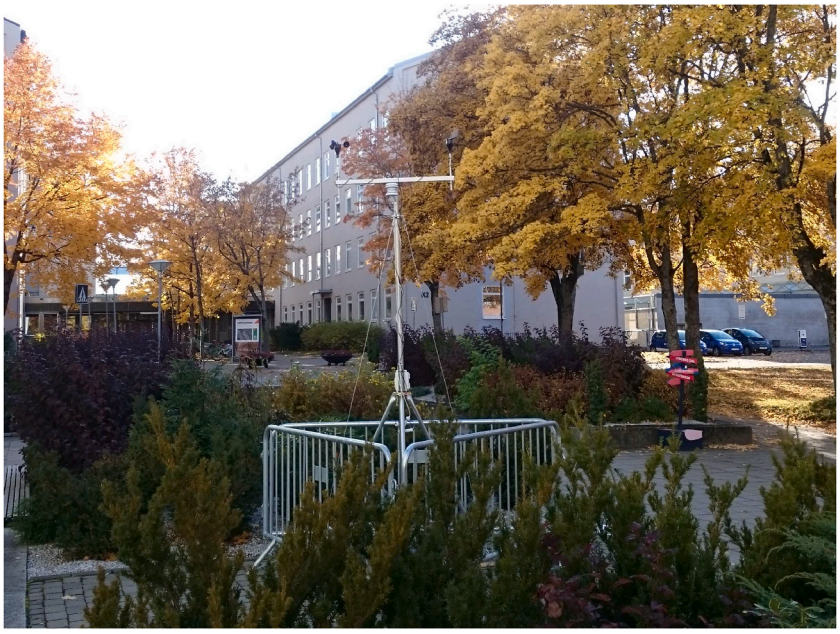

Fig. 4. A mobile weather station at NTNU's Gløshaugen campus in October 2019.

2.2. CFD-BPS coupling

In this study, a CFD (*ANSYS Fluent 2020 R1*) and BPS tool (*IDA ICE 4.8 SP2*) are coupled to study the influence of different compositions of the urban surface on building energy demand during different times of the year. *ANSYS Fluent* is a widely used CFD simulation and physical modeling software with a wide range of applications. It has been applied in many previous studies of the urban microclimate [96,97] and the coupling with BPS (see Table 1). *IDA ICE*, on the other hand, is a dynamic multi-zone simulation software for studying the thermal indoor climate as well as the energy demand of a building [98,99]. It has been validated with respect to several standards [100–102] and can be used to model for instance double-skin façades [103,104], boreholes [105], or advanced control strategies of heat pumps [106,107], among other things. The settings and boundary conditions for the CFD and BPS model used in this study can be found in chapters 3 and 4, respectively. The coupling strategy, according to the terminology used in section 1 in this article, is a one-way coupling of type B. Consequently, the results from the CFD simulations are used as input for BPS (Fig. 2). Additional climate variables that are required for BPS are taken from the reference weather station (RWS) at the campus. The following microclimate scenarios (MS) are investigated in CFD:

1. *Base case (MS-Base)*: actual situation.
2. *No vegetation (MS-NoVeg)*: no trees, all vegetated ground surfaces substituted with concrete.
3. *All vegetation (MS-AllVeg)*: all ground surfaces substituted with grass.
4. *"High-Performance Neighborhood" (MS-HPN)*: All explicitly modeled buildings surrounding the building of interest (SB1) with high-performance building envelope (0.3 m insulation and exterior charred wood cladding).

The four MSs are simulated for three 168-h (1 week) simulation periods (SP) in different seasons of the year, namely summer, autumn, and winter. The terminology used in the remainder of this article and the dates of these SPs are SUM (June 15 00:00:00 – June 21 23:59:59), AUT (September 16 00:00:00 – September 22 23:59:59), and WIN (December 21 00:00:00 – December 27 23:59:59) for summer, autumn, and winter 2020, respectively (see also Fig. 2). From BPS, the heating energy demands during AUT and WIN are obtained. For SUM, the cooling energy demand and the number of hours in which the operative temperature (T_{op}) in the zones exceeds 26 °C ($N_{T_{op}>26\,^{\circ}C}$) are compared.

Although *MS-HPN* addresses the microclimatic situation with a district-wide high-performance building envelope, the building envelope of the building of interest (SB1) is not changed to ensure comparability between the scenarios. The microclimatic conditions in these scenarios are logged in *ANSYS Fluent* in close vicinity to SB1 at overall 43 logging points (Fig. 3a). Always seven of these logging points are lined up vertically in front of each building façade to log air temperature. The spacing between the measurement points is 6 m (two stories), the distance between the points and the building surface is 2 m. Due to the oblong shape of the building, the façades towards the northwest and southeast have two lines with points in front of them. A 43rd point, centrally located 3 m above the roof of the building is used to log wind speed and wind direction. The collected data are used to create the weather files for BPS. It is accounted for a changing air temperature $T_a(z)$ over the height of the building, where z is the height above ground. For that, separate weather files with an air temperature calculated as a mean of all data extraction points with the same z (6 m, 12 m, etc.) are created and assigned to always two building floors at about the same height. A more detailed description of the procedure is outlined in section 4.2.

Furthermore, the CFD model is used to determine the pressure coefficients C_p [−] on each façade of the investigated building which

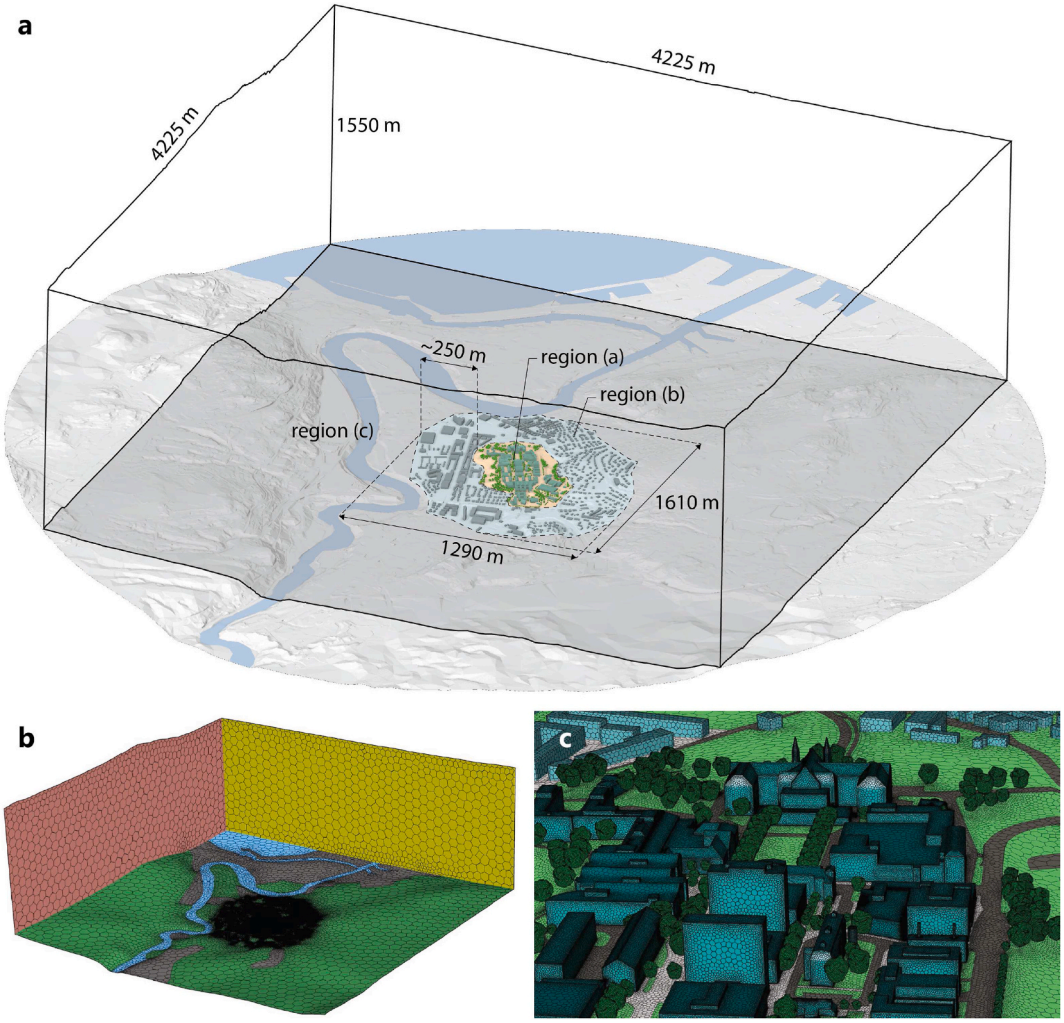

Fig. 5. Computational domain (4225 × 4225 × 1550 m^3) with 9,123,834 cells; (a) Domain boundaries viewed from the south-east with different geometrical modeling regions and dimensions; (b) Meshed domain with different surface types: water (blue), primarily green spaces (green), densely built-up or industrial areas (grey), northern (yellow) and western (red) boundary; asphalt (dark grey), concrete/pavement (light grey); (c) Close-up view of the NTNU campus buildings and trees and different surface types: asphalt (dark grey), concrete/pavement (light grey) and green spaces (green). (For interpretation of the references to colour in this figure legend, the reader is referred to the Web version of this article.)

are then exported to the BPS tool (see Fig. 2). Eq. (1) shows the calculation procedure for C_p, where P_x [Pa] is the static pressure at a specific point on the building façade, P_0 [Pa] is the freestream static reference pressure, and P_d [Pa] is the dynamic pressure at freestream which is calculated from Eq. (2). There, ρ [kg m^{-3}] is the density of air, and U [m s^{-1}] is the wind speed, often taken at

Table 3
Wall structure of buildings and the urban surface for the CFD simulations.

Building categories/Urban surface	Layer 1 (adjacent to fluid cells)		Layer 2		Layer 3 (domain's exterior)	
	Material	d [m]	Material	d [m]	Material	d [m]
I (Wood)	Wood: spruce	0.05	Insulation	0.25	Wood: spruce	0.05
II (Stone)	Granite	0.2	Brick	0.2	–	–
III (Brick)	Brick	0.36	–	–	–	–
IV (Concrete, old)	Concrete	0.36	–	–	–	–
V (Concrete, new)	Plaster	0.02	Insulation	0.2	Concrete	0.2
Surrounding buildings	Brick	0.3	–	–	–	–
Roads	Asphalt	0.3	Granite	1.0	Earth	8.7
Pavement	Concrete	0.3	Granite	1.0	Earth	8.7
Grass	Earth	0.01	Earth	0.49	Earth	9.5

Symbols: Material layer thickness (d).

Table 4
Selected optical and thermal properties of the surface materials on campus [7,124,130,131].

Surface	α [−]	ε [−]	c [kJ kg^{-1} K^{-1}]	δ [kg m^{-3}]	λ [W m^{-1} K^{-1}]
Wood: spruce	0.75	0.90	2310	700	0.17
Wood: spruce (charred)	0.93	0.95	2310	700	0.17
Asphalt	0.70	0.95	800	2400	0.75
Concrete	0.66	0.95	1000	2300	1.60
Plaster	0.66	0.95	1000	1800	1.00
Insulation (not a surface material)	–	–	840	50	0.05
Granite	0.70	0.95	790	2800	3.00
Earth (covered with grass)	0.77	0.95	1000	1400	1.80
Brick	0.66	0.95	900	2050	0.80

Symbols: Shortwave absorptivity (α), emissivity (ε), heat capacity (c), density (δ), thermal conductivity (λ).

building roof level in the upstream undisturbed flow. Pressure coefficients are determined for the eight standard wind directions for every surface of the building envelope. In this study, the data extraction points for the freestream flow variables P_0 and P_d are stipulated at 100 m distance from the building of interest in the respective wind direction (Fig. 3b). A rather large distance to the building was chosen in order to capture the freestream flow variables that are not affected by the upstream wind-blocking effect [108–110].

$$C_p = \frac{P_x - P_0}{P_d} \tag{1}$$

$$P_d = \frac{\rho U^2}{2} \tag{2}$$

The standard procedure in BPS tools is usually to use generic pressure coefficients and in the case of *IDA ICE*, from the AIVC database, based on a specified wind profile and building density of the surrounding environment [111,112]. Local effects from close buildings and vegetation, however, are not included in this standard procedure. Considering the vicinity of the SB2 high-rise building to the northwest these effects are important and require a closer examination, for instance by using CFD.

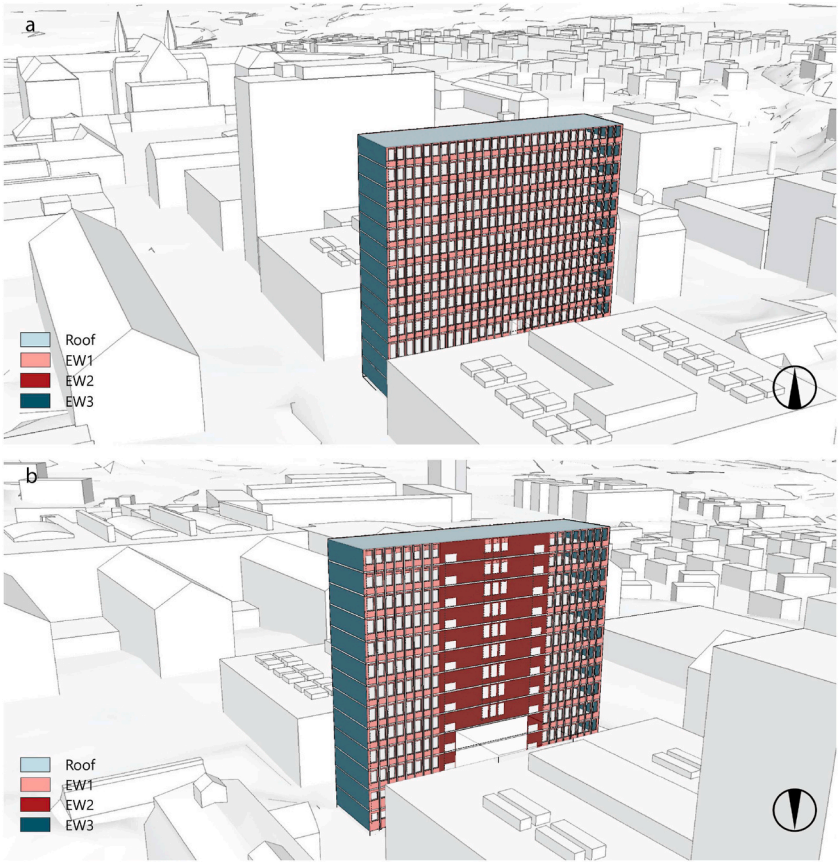

Fig. 6. Different constructions used in the IDA ICE BPS model. (a) View of SB1 from the south; (b) View of SB1 from the north.

3. CFD model design and settings

3.1. Measurement campaign for CFD model validation

From September 23 to October 21, 2019, a measurement campaign was conducted to record the microclimatic conditions at the campus. A network of five mobile weather stations (see Fig. 4) that recorded air temperature, relative humidity, wind speed, and direction in 0.1 Hz intervals at a height of 3 m was used. Additionally, a fixed weather station, 10 m above the roof of the VATL building (28 m above the ground, see Fig. 1) was used as the RWS for calibration. There, global horizontal radiation was measured in addition to the previously mentioned climate variables. The recorded climate variables from the RWS served as a basis for the input at the domain boundaries in the CFD simulations.

The validation was carried out for two 48-h periods during the measurement campaign which were September 27–28 and October 19–20. In general, both periods featured a strong variability in meteorological conditions regarding wind speed, wind direction, air temperature, and global horizontal radiation. The goal of selecting these dates was to investigate the CFD model's performance under variable and fluctuating conditions. Further information about the measurement campaign, as well as the CFD model's performance can be found in a separate study entirely dedicated to the CFD model validation process [113].

3.2. Computational domain and features

The computational domain (4225 × 4225 × 1550 m^3) of the study area features regions of three different types of geometrical modeling (Fig. 5a): (a) where buildings and trees are represented explicitly with a rather high level of details (NTNU campus), (b) the area around the NTNU campus, where only buildings and no vegetation are represented explicitly yet with a lower degree of detail (representation of buildings as simple boxes), and (c) the wider surroundings of the area of interest which are only represented implicitly by assigning an aerodynamic roughness length z_0 according to the Davenport-Wieringa roughness classification [114]. A grid convergence study was performed, and the selected mesh is a poly-hexcore grid that consists of 9,123,834 cells (see Fig. 5b and c).

The 3D unsteady Reynolds Averaged Navier Stokes (URANS) equations are solved for which the realizable k-ε turbulence model [115] provides closure. This turbulence model was reported to have good performance for wind flow around buildings [34,109,116] and has been successfully applied in many validated CFD studies of the urban microclimate [80,84,85,96,117]. The exchange of long-wave radiation is included by employing the Discrete Ordinates radiation model [118,119]. This model's angular discretization settings are kept at the standard value of 2 for the number of theta and phi divisions, and 1 for the number of theta and phi pixels. The SIMPLEC [120] algorithm is employed for the pressure-velocity coupling and schemes of second-order only are used for the spatial discretization. More detailed information about the computational settings and validation of the CFD model can be found in a separate article by Brozovsky et al. [113].

The CFD model furthermore features natural convection, solar radiation and longwave radiation exchange, heat storage in the urban surface, the thermal effects from evapotranspiration at grass surfaces (Penman-Monteith equation [121–124]) and the thermal effects from evaporation and aerodynamic effects at trees [117,125–129]. However, it is a purely *dry* model and thus does not include relative humidity or the phase change behavior of water due to its large needs in computational power. The Leaf Area Density of the trees is an important parameter to consider in and indicates the area of leaves per cubic meter of tree crown [$m^2\ m^{-3}$]. Due its seasonal variability, it is set to 1.5 m^{-1} for SUM, 1.0 m^{-1} for AUT, and 0.2 m^{-1} for WIN in the model equations (see also Brozovsky et al. [113]). The latter value is not set to zero, although the trees have no leaves during this SP. However, with a value of 0.2 m^{-1}, the aerodynamic effect especially of the trees' branches is approximated. The evapotranspirational cooling potential on the other hand was set to zero during WIN.

All ground surfaces were modeled with a thickness of 10 m using shell conduction in *ANSYS Fluent*. With this approach, heat storage and conduction both in the normal and planar direction are considered. At 10 m, a constant temperature according to groundwater temperature measurements near the study site is assigned. These temperatures are 4.2 °C, 5.0 °C, and 5.8 °C for SUM, AUT, and WIN, respectively. There is a strong seasonal shift of approximately 6 months between maximum air temperature and groundwater temperatures which results in higher ground temperatures in the winter months than in summer.

The water-covered areas, namely the river *Nidelva* and *Trondheim Fjord* are not modeled as a fluid but as a "thin wall" with surface

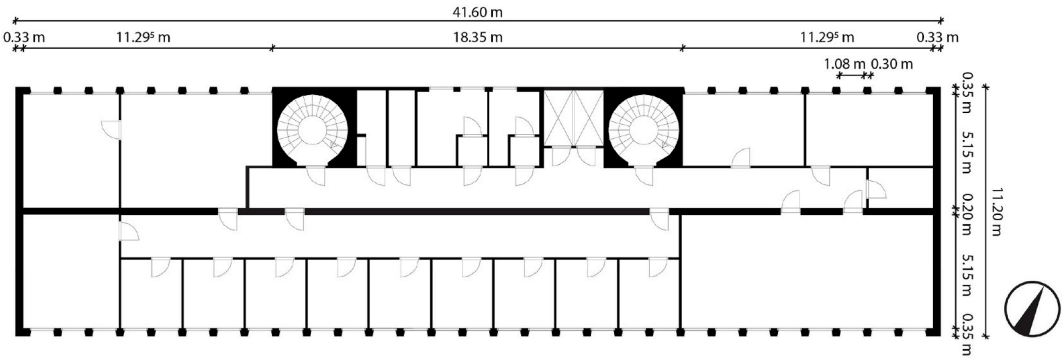

Fig. 7. Typical floor plan and dimensions of SB1.

Table 5
Wall structures used for SB1 from the inside (layer 1) to the outside (layer 4) in the BPS simulations.

Envelope surface	Layer 1 (inside)			Layer 2			Layer 3			Layer 4 (outside)			U-value
	Material	d	λ	Material	d	λ	Material	d	λ	Material	d	λ	[W m^{-2} K^{-1}]
EW1	Gypsum	0.013	0.22	Rockwool	0.1	0.04	Concrete	0.05	2.5	Render	0.025	0.8	0.36
EW2	Render	0.015	0.8	Cork	0.05	0.05	Concrete	0.4	2.5	Render	0.025	0.8	0.73
EW3	Render	0.015	0.8	Aerated concrete	0.15	0.14	Concrete	0.18	2.5	Render	0.025	0.8	0.73
Roof	Render	0.015	0.8	Concrete	0.16	2.5	Rockwool	0.14	0.04	Ventilated air cavity[a]			0.27

Symbols: Material layer thickness d in [m]; thermal conductivity of materials λ in [W m^{-1} K^{-1}] from [131].
[a] Thermally not relevant.

water temperatures obtained from Sea and Land Surface Temperature Radiometry onboard the European Space Agency's Copernicus Earth monitoring system of the Sentinel-3 satellites. These satellite images have a resolution of 1 km^2 and provide the input at the simulated times of the year. The temperatures used as BC are 18.5 °C for SUM, 11.4 °C for AUT, and 4.8 °C for WIN.

The material layers of the building categories and the urban surface are listed in Table 3. Table 4 lists the optical and thermal properties of the surface materials that are used in the model and were assumed to be constant in this study. In *MS-HPN*, the envelope insulation properties of all explicitly modeled buildings surrounding SB1 were improved. SB1 on the other hand remained unchanged. In this scenario, buildings which in the base case scenario were not modeled with an insulation layer, such as categories II, III, IV, and the surrounding buildings were equipped with 0.3 m of insulation and a 0.05 m charred wood cladding to the exterior of the building, adjacent to the fluid cells of the domain. In the remaining building categories I and V, the existing insulation layer was increased to 0.3 m, and a 0.05 m charred wood cladding is added to the outside of the building, adjacent to the fluid cells of the domain. In building category I, the existing wood cladding is replaced by charred wood.

In this study, three 168-h periods are simulated with 1-h time steps and 400 iterations per time step except for the first one, for which 800 iterations were performed to provide better convergence. As a consequence, in total 168 time steps with 67,600 iterations are carried out for each of the three 168-h periods. On average, the following scaled residuals are reached at the end of each time step: 2.1×10^{-5} for continuity, 1.8×10^{-4} for x-velocity, 2.2×10^{-4} for y-velocity, 1.6×10^{-4} for z-velocity, 5.8×10^{-4} for k, 1.6×10^{-3} for ε, 9.6×10^{-8} for energy, and 1.1×10^{-6} for radiation. The computations took on average about 1.5 h in real-time per simulated hour on a high-performance computer cluster using five nodes of 30 Intel® Xeon® E5-2683 v4 central processing units @ 2.10 GHz each.

A more detailed description of the CFD model can be found in a separate article by Brozovsky et al. [113]. There, the geometrical data sources and modeling techniques of the complex terrain, the description and results of a grid-convergence study, and other computational settings and boundary conditions are explained in detail. However, it is worth noting that the CFD model was created in accordance to the best practice guidelines by Franke et al. [132] and Tominaga et al. [133].

4. BPS model design and settings

4.1. Building specifications

The building of interest, an office high-rise, is part of the *Sentralbygg* (English: *Central Building*) complex, in the middle of the NTNU campus. This building complex comprises two high-rises and three low-rise buildings (see Figs. 3 and 6). SB1 is axially aligned with the main Gløshaugen development which is rotated ca. 335° from the north. SB1 was constructed in 1961 with a concrete skeleton as the bearing structure and is 40 m high. It has a GFA of ca. 6000 m^2 and the ceiling height is 3.0 m, with exception of the 1st and 2nd floors which are 3.2 m high. The exterior walls show a regular window grid, consisting of 29 window columns, each between load-bearing columns on the south-eastern façade. To the northwestern side, the same grid applies, with exception of the building core which consists of two staircases, an elevator shaft, restrooms, and other technical rooms (see Fig. 7). Besides the roof, the insulating materials

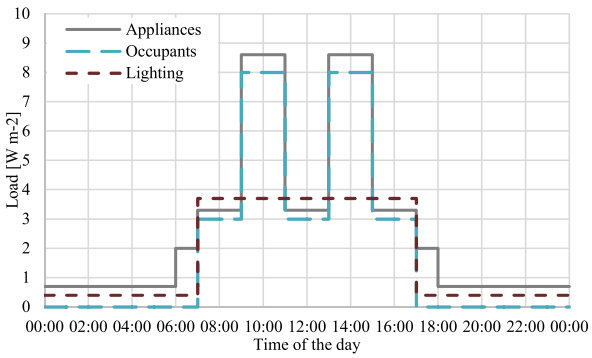

Fig. 8. Internal gains on weekdays for an office building according to SN-NSPEK 3031:2020 [134].

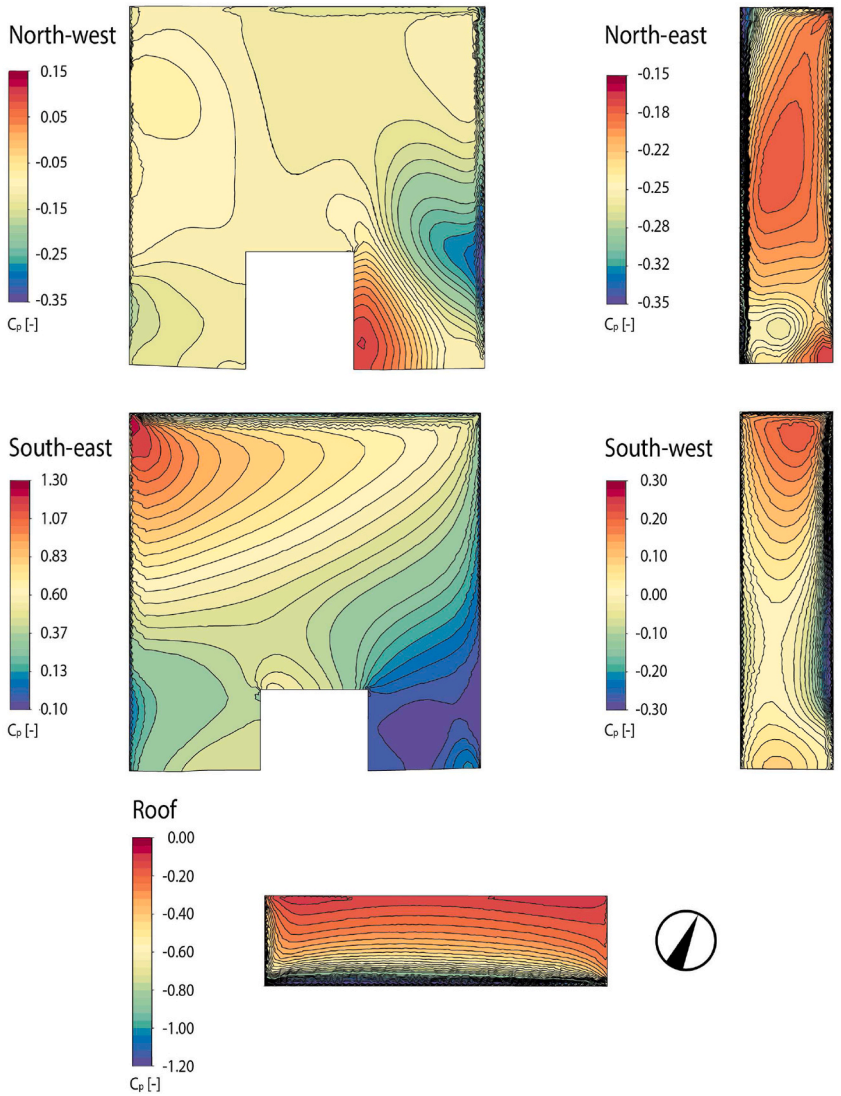

Fig. 9. Pressure coefficients C_p on the building envelope surfaces of the building of interest (SB1) at southerly wind.

are located on the inside of the bearing structure. There are three types of external walls (EW): (EW1) prefabricated wall panels with 10 cm interior rock wool insulation between the columns (on the south-eastern and the northwestern façade apart from the building core), (EW2) a thick concrete wall with 5 cm of internal cork insulation (building core between the staircases), and (EW3) the gable walls with 15 cm aerated concrete blocks on the inside (see Table 5). Moreover, the building features two different types of windows. On the northwestern side of the building, triple-glazing insulating windows are installed (U-value incl. frame: 0.93 W m^{-2} K^{-1}; g-value: 0.60 according to manufacturer's datasheet), while on the south-eastern side, double-glazing windows with integrated Venetian blinds and a protecting third glass pane on the outside are mounted (U-value incl. frame: 1.30 W m^{-2} K^{-1}; g-value: 0.52 according to

Table 6
Façade-averaged pressure coefficients C_p for the eight investigated wind directions. The relative frequency of each wind direction at the RWS during the three investigated weeks in % is given in brackets below the wind direction.

Façade (azimuth)	Wind direction [°] (relative frequency [%])							
	0° (3.4%)	45° (0.2%)	90° (0.2%)	135° (4.8%)	180° (44.0%)	225° (21.6%)	270° (7.3%)	315° (18.5%)
North-east (65°)	−0.09	0.23	0.35	−0.09	−0.22	−0.18	−0.14	−0.16
South-east (155°)	−0.21	−0.30	0.02	0.51	0.42	−0.09	−0.18	−0.11
South-west (245°)	−0.28	−0.25	−0.23	−0.20	0.01	0.36	0.21	0.02
North-west (335°)	0.14	−0.09	−0.31	−0.07	−0.12	−0.27	0.06	0.17
Roof (−)	−0.44	−0.39	−0.43	−0.40	−0.43	−0.37	−0.28	−0.24

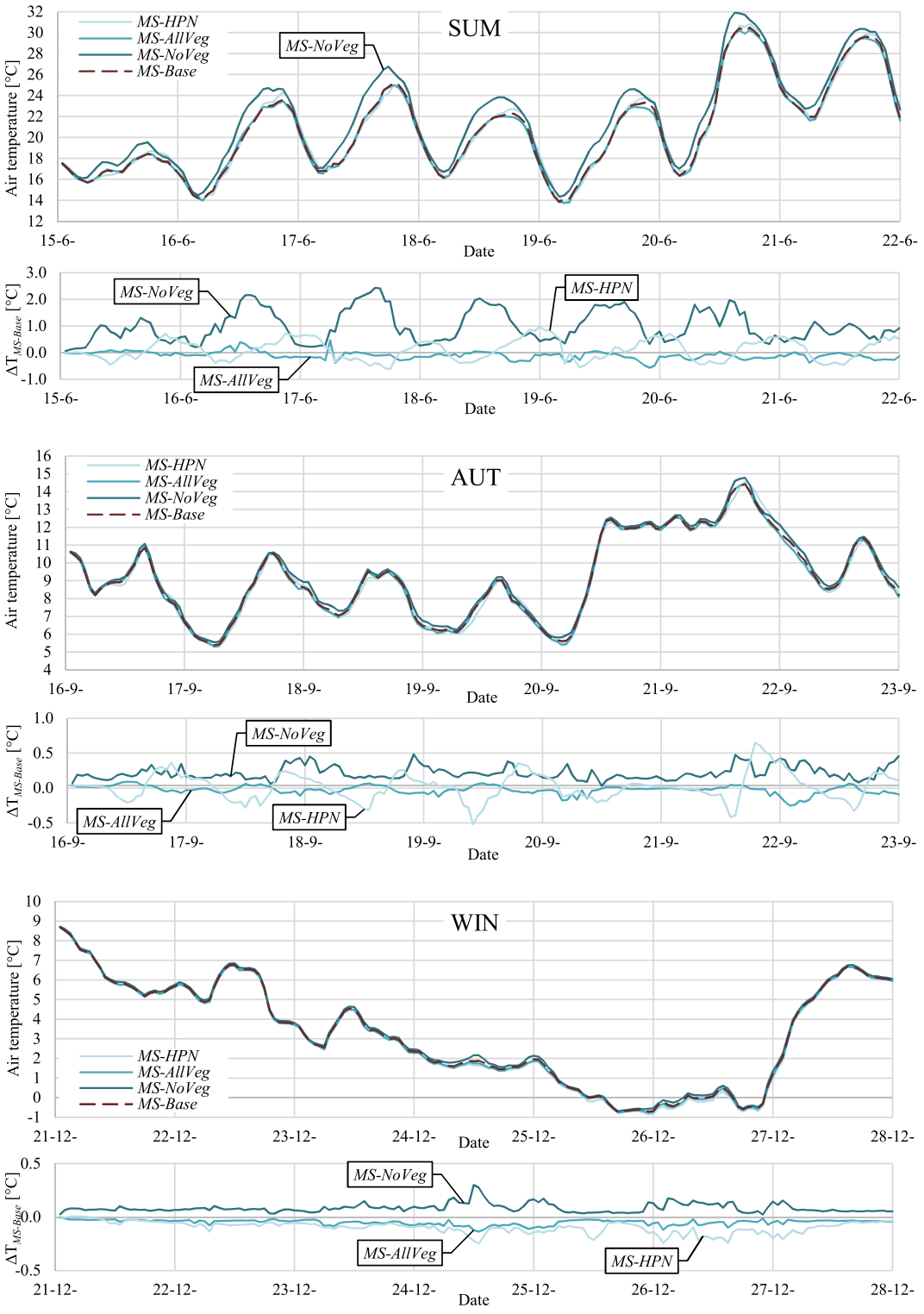

Fig. 10. Air temperature of the different MSs and air temperature difference of MS-NoVeg, MS-AllVeg, and MS-HPN compared to MS-Base during SUM, AUT, and WIN as an average of the 42 logging points around the building of interest (SB1).

Table 7
Key figures of the air temperatures at SB1 from the CFD simulations and time of occurrence where applicable.

SP	MS	T_{min}		T_{max}		T_{avg}	ΔT_{low}		ΔT_{high}		ΔT_{avg}
		[°C]	time	[°C]	time	[°C]	[°C]	time	[°C]	time	[°C]
SUM	*Base*	13.9	19.06.04:00	30.5	20.06.18:00	20.7	–	–	–	–	–
	NoVeg	14.4	19.06.04:00	31.9	20.06.15:00	21.7	0.1	15.06.01:00	2.4	17.06.15:00	1.0
	AllVeg	13.8	19.06.05:00	30.3	20.06.18:00	20.6	−0.6	19.06.22:00	0.5	17.06.06:00	−0.1
	HPN	13.7	19.06.05:00	30.8	20.06.18:00	20.8	−0.6	17.06.18:00	1.0	19.06.00:00	0.1
AUT	*Base*	5.4	17.09.06:00	14.4	21.09.17:00	9.2	–	–	–	–	–
	NoVeg	5.5	17.09.06:00	14.8	21.09.17:00	9.4	0.0	20.09.12:00	0.4	18.09.22:00	0.2
	AllVeg	5.3	17.09.06:00	14.4	21.09.17:00	9.2	−0.3	22.09.02:00	0.1	16.09.12:00	−0.1
	HPN	5.3	17.09.06:00	14.6	21.09.17:00	9.2	−0.6	19.09.10:00	0.6	21.09.19:00	0.0
WIN	*Base*	−0.7	25.12.17:00	8.7	21.12.01:00	3.2	–	–	–	–	–
	NoVeg	−0.7	25.12.17:00	8.7	21.12.01:00	3.3	0.0	26.12.22:00	0.3	24.12.12:00	0.1
	AllVeg	−0.8	25.12.23:00	8.7	21.12.01:00	3.1	−0.1	24.12.13:00	0.0	21.12.01:00	0.0
	HPN	−0.9	25.12.23:00	8.7	21.12.01:00	3.1	−0.2	24.12.13:00	0.0	21.12.04:00	−0.1

Symbols: Minimum air temperature (T_{min}), maximum air temperature (T_{max}), average air temperature (T_{avg}), largest lower deviation to *MS-Base* (ΔT_{low}), largest higher deviation to *MS-Base* (ΔT_{high}), and average deviation to *MS-Base* (ΔT_{avg}).

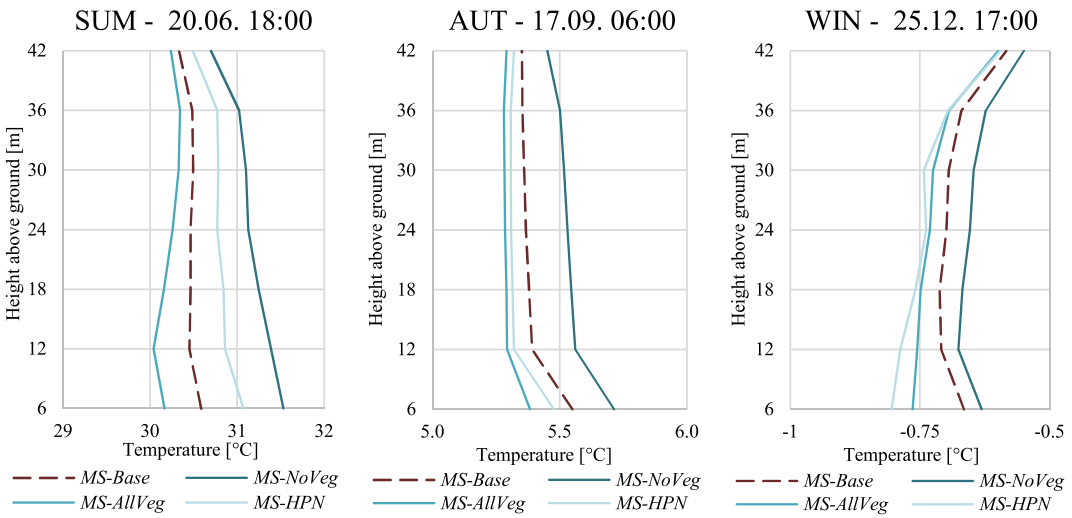

Fig. 11. Temperature profiles showing the air temperature averages according to the logging point heights around SB1 for all MSs at selected times of the day during SUM (20.06. at 18:00), AUT (17.09. at 06:00), and WIN (25.12. at 17:00).

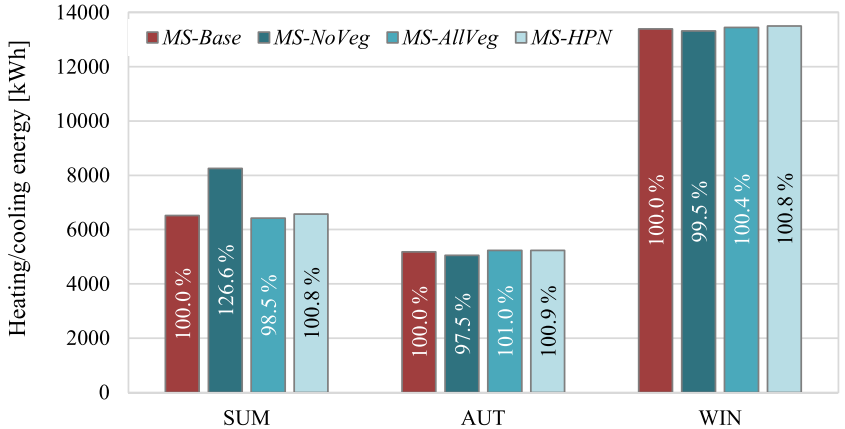

Fig. 12. Total heating (AUT and WIN) and cooling (SUM) energy demand of SB1 during the investigated SPs.

manufacturer's datasheet). As mentioned in the methodology section, the same BPS model is used for all investigated scenarios.

4.2. Other BPS settings

The operating schedules and internal loads for the BPS are taken from the Norwegian standard SN-NSPEK 3031:2020 [134] for the building category *Office building* (Fig. 8). In accordance with NS 3031:2014 [135], the operation times for mechanical ventilation and room heating are from 07:00–19:00 during the weekdays. For room heating, the setpoints are 21 °C and 19 °C during and outside of the operational hours, respectively. The mechanical ventilation system (constant air volume) supplies the zones with 7 $m^3\ m^{-2}\ h^{-1}$ and 2 $m^3\ m^{-2}\ h^{-1}$ during and outside of the operational hours, respectively [134]. From the ventilation system, in which a rotary heat recovery unit with 70% efficiency pre-conditions the incoming air, the zones are supplied with air at constant 19 °C. With only a heating and no cooling coil installed, the supply air temperature can get higher in summer when the outdoor air temperature exceeds 19 °C. The interior insulation and poor prevention of thermal bridges cause a normalized thermal bridge factor of ca. 0.20 $W\ m^{-2}\ K^{-1}$. It needs to be pointed out that this factor is based on the gross internal area of buildings in Norway, not the envelope area. The

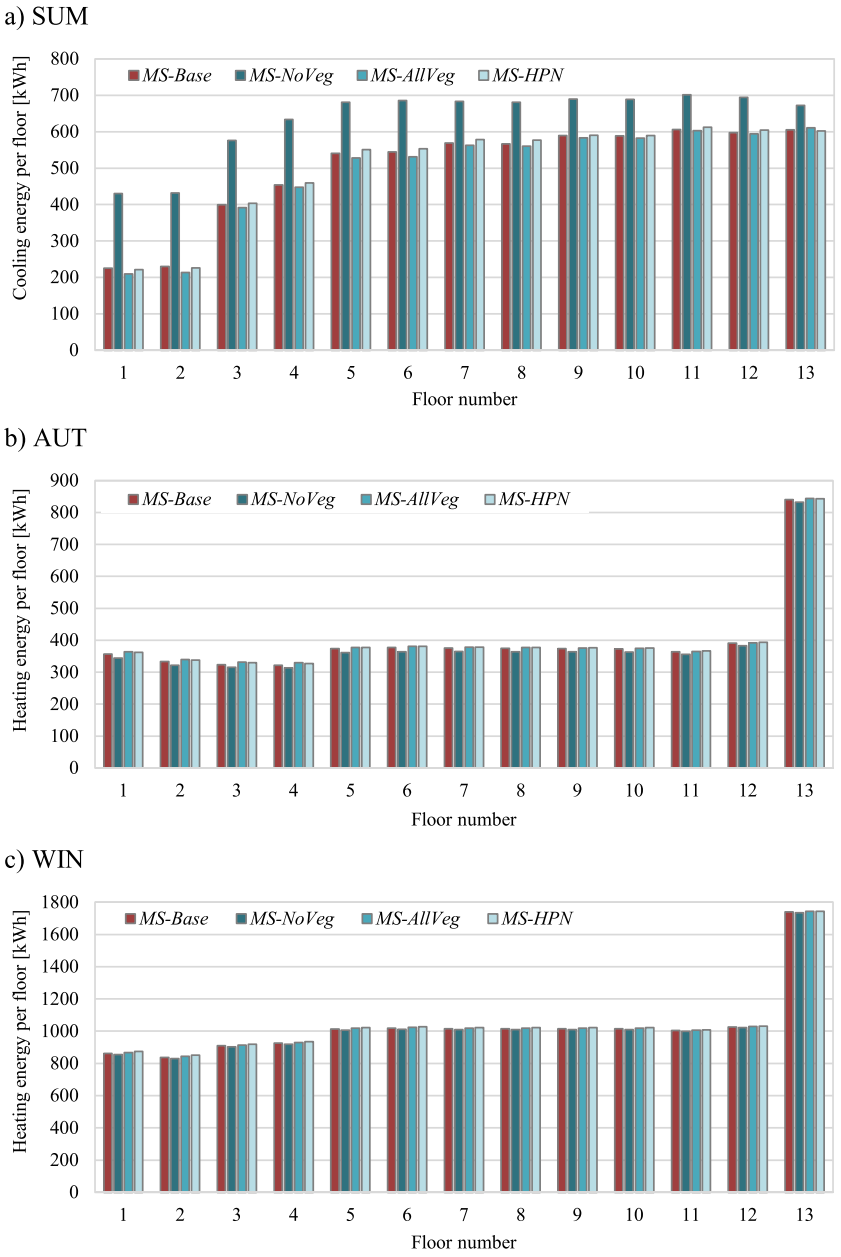

Fig. 13. Energy demands of the simulated scenarios in the SPs per floor. a) cooling energy demand in SUM; b) heating energy demand in AUT; c) heating energy demand in WIN.

infiltration rate is assumed to be 3.0 h^{-1} at 50 Pa pressure difference [136]. In the simulation model, a control strategy is added for the operation of the window-integrated Venetian blinds. Following NS 3031:2014 [135], it is modeled so that the blinds are pulled down when solar irradiation on the outside of the window exceeds 100 W m^{-2} in WIN, and 250 W m^{-2} in SUM and AUT. No window opening control strategy is implemented as the building has a mechanical ventilation system to ensure the required ventilation rates and user behavior related to operating windows in buildings is very complex [137]. Equally important, the Norwegian standards that are used for the calculation of a building's energy performance do not provide for windows to be opened. Domestic hot water is not considered in this study.

Furthermore, every floor was modeled as a single zone. Because the used standards require using the same internal loads irrespective of the specific usage of a room (e.g. office, hallway, meeting room), a finer segmentation of zones would not increase the accuracy of the simulation model but prolong simulation times. To determine the energy demand, an ideal heating element that is capable of providing enough thermal energy to reach the desired heating setpoints at any time is placed in every zone. In this way, the obtained demand is independent of the system type and comparability is facilitated. The SUM simulations were carried out in two different ways: (1) with ideal cooling elements to be able to compare hypothetical cooling loads, and (2) no ideal cooling elements in the zones, as the real building does not have a cooling system installed. While in case 1, the energy demand for cooling in kWh is compared, case 2 shows a comparison of the number of hours in which the T_{op} in the zones exceeds 26 °C ($N_{T_{op}>26\,°C}$). The latter is a metric used for documenting the quality of indoor thermal comfort for summer periods according to the Norwegian building code [138].

Furniture, internal walls, and structures such as the building core and staircases are considered as thermal mass in every zone. Because the influence of the microclimatic conditions on the building's basement is negligible, it is not taken into consideration in this study. Therefore, the BC of the floor towards the basement is set to adiabatic.

The pressure coefficients are determined from CFD simulations and used in the BPS (see section 5.1). However, *IDA ICE* requires the specification of an exponential wind profile (see Eq. (3)) which is applied to the wind speed from the climate file. From that, the wind speed at any height $U(z)$ [m s^{-1}] is determined. In this equation, $U_{ref,CFD}$ [m s^{-1}] and $z_{ref,CFD}$ [m] are the wind speed and height at which the wind speed was extracted from the CFD simulations. There, $z_{ref,CFD}$ is 45 m and a_0 [−] and a_{exp} [−] are assumed to be 0.67 and 0.25, respectively, based on Liddament's guide on air infiltration calculation techniques [111] for the terrain category *urban, industrial, or forest areas*.

$$U(z) = U_{ref,CFD}\ a_0 \left(\frac{z}{z_{ref,CFD}}\right)^{a_{exp}} \tag{3}$$

A two-week startup period, using recorded climate data from the RWS, ensures that the impact of the initial value at the start of a simulation is minimized. In BPS, weather files usually contain only one global outdoor air temperature. In this study, the BPS model has been modified to account for a changing air temperature over height $T_a(z)$. Floors 1 and 2 have been assigned the average of all extracted outdoor air temperatures extracted from CFD at 6 m height, floors 3 and 4 that of 12 m, etc. Finally, the 13th floor is assigned the extracted outdoor air temperature at 42 m. The change of outdoor air temperature was only considered in a vertical direction. Although data for the different temperatures at the individual façades of SB1 was available, no further segmentation of climatic BC was undertaken. The additional modeling necessary for façade-specific, temperature BC is extremely time-consuming and does not improve accuracy if all lateral building surfaces are adjacent to the same zone as in the present study.

5. Results

5.1. Pressure coefficients

The distribution of pressure coefficients C_p on each of the investigated building's envelope surfaces is presented in Fig. 9. The situation is shown for wind from the south, as during the three investigated weeks it was the most common wind direction (44.0% of the time or 222 h in total). As visible in Fig. 9, the pressure distribution on the building envelope surfaces is heterogenic, presenting large gradients especially at the corners of the building. The pressure coefficients ranged from −1.20 at the southern edges of the roof to 1.30 at the upper left corner of the southeastern facade. Particularly at the roof, the northeastern and southwestern façade, the respective minimum values occur at the edges that are shared with the southeastern façade. In these locations, flow separation is observed which evokes large gradients, visualized by narrow contour lines at the edges. In this study, the standard approach using façade-averaged pressure coefficients was employed. The façade-averaged pressure coefficients for each of the eight investigated wind directions are listed in Table 6.

5.2. CFD microclimate simulations

Since the used CFD model has been validated in detail and found suitable to be used for microclimate studies in a separate study by Brozovsky et al. [113], no further validation process will be reported at this point. However, comparing the results from the simulated base case scenario (*MS-Base*) to the measurements at the RWS in the respective SPs, similar model accuracies were obtained as in the article dedicated to the model validation. In the remainder of this article, the average air temperature from the 42 logging points around the building of interest (SB1) will be referred to as *air temperature at SB1*, as opposed to the *air temperature at the RWS* which is logged at the location of the RWS, 10 m above the VATL building.

In Fig. 10, the air temperatures at SB1 for the different MSs during SUM, AUT, and WIN are presented. Furthermore, the differences in air temperature $\Delta T_{MS-Base}$ at SB1 of *MS-NoVeg*, *MS-AllVeg*, and *MS-HPN* compared to *MS-Base* are illustrated. While in SUM quite pronounced differences between the MSs can be observed, particularly with regard to *MS-NoVeg*, the investigated MSs have a fairly

small impact on air temperature during AUT and WIN. This tendency can be explained by the seasonal availability and intensity of solar radiation onto the urban surface. While during SUM, the solar elevation angle is rather high and days are long, the urban surface is able to absorb a lot of energy from solar radiation. Towards WIN, the situation reverts.

In all three SPs, *MS-NoVeg* shows the largest variation of microclimatic conditions with an air temperature that almost continuously surpasses that of *MS-Base*. During SUM, when the daily temperature maxima in *MS-Base* are reached (typically around 18:00–20:00), the differences are most pronounced. Other metrics and key figures of the three SPs are given in Table 7. From there, it can be seen that the simulated air temperatures at SB1 for *MS-NoVeg* are on average 1.0 °C, 0.2 °C, and 0.1 °C warmer than in *MS-Base* in SUM, AUT, and WIN, respectively. On the other hand, *MS-AllVeg* is on average 0.1 °C cooler than in *MS-Base* in both SUM and AUT. In WIN, the average temperature remained close to unchanged. While *MS-HPN* is 0.1 °C warmer than *MS-Base* during SUM, there is only little influence on air temperature at SB1 during AUT and WIN. In *MS-NoVeg*, up to 2.4 °C higher air temperatures are obtained in SUM, while the maximum difference is 0.4 °C in AUT and 0.3 °C in WIN. In *MS-AllVeg*, the additional greening led to a maximum decrease in air temperature of 0.6 °C during SUM and 0.3 °C during AUT, while in WIN, it was 0.1 °C.

MS-HPN on the one hand led to relatively large reductions of air temperature at certain points in time with a maximum of 0.6 °C during SUM and AUT, and 0.2 during WIN, but also caused significant air temperature increases at other times. These maximum increases were 1.0 °C and 0.6 °C during SUM and AUT, respectively. It is furthermore noticeable that there is a strong diurnal variation in air temperature differences between MS-HPN and MS-Base. While during the day, this difference first begins to decrease and eventually becomes negative during the morning, it becomes positive again during the late afternoon until the next morning.

Fig. 11 shows the air temperature at SB1 for the different MSs at selected points in time, averaged and plotted with respect to the logging points' height above the ground. It can be seen that the differences between the temperature profiles are larger close to the ground and that they converge with increasing height. It is also noticeable that with the transition from summer to winter, the differences between the MSs of an SP get smaller. The temperature profiles for SUM present the situation at the point in time where the air temperature at SB1 reaches its maximum in *MS-Base* (20.06.18:00). In *MS-Base*, the temperature profile shows the least variation over the height of SB1 with a mean of 30.5 °C. Large differences can be identified especially with regard to *MS-NoVeg* and *MS-AllVeg*. The notch in all scenarios but *MS-NoVeg* at 12 m height can be attributed to close-by trees at this height. Depending on the wind direction, this indentation is sometimes more, sometimes less pronounced.

During AUT, the minimum air temperature of *MS-Base* is obtained on 17.09. at 06:00. At this point in time, the difference between all scenarios is rather small. On Dec 25, at 17:00, the coldest point in time during WIN and of all SPs, *MS-HPN* has the lowest air temperatures at SB1. The better insulation of the building envelopes leads to fewer heat losses which are particularly noticeable close to the buildings. Additionally, very little solar radiation during WIN leads to a generally smaller influence from the materials of the urban surface.

5.3. Building performance simulations

The influence of the local microclimate conditions on building energy demand is strongly in line with the results from the CFD simulations where the differences were largest in SUM and smallest in WIN. Fig. 12 shows the total heating/cooling energy demand of the four MSs in every SP. Resulting from the large temperature differences between *MS-NoVeg* and *MS-Base* in the CFD simulations during SUM, the absence of green infrastructure as in *MS-NoVeg* in Trondheim during the simulated week in June 2020 would have increased the cooling energy demand in SB1 by 26.6%. At the same time, an entirely greened urban surface as in *MS-AllVeg* would have reduced the cooling energy demand by 1.5% compared to the current situation. Improving the insulation level of the buildings surrounding SB1 in *MS-HPN* led to a slight increase of cooling energy demand by 0.8%. In this scenario, a lower albedo of the building envelopes leads to more absorbed radiation and thus higher surface temperatures. Consequently, due to higher convective heat exchange with the environment, higher outdoor air temperatures are observed.

On the other hand, in both AUT and WIN, *MS-NoVeg* represents the scenario with the lowest energy demand. As in both SPs, outdoor temperatures require the building to be actively heated, slightly higher outdoor temperatures from an urban surface without greening result in reduced heating demands. These reductions add up to 2.5% and 0.5% in AUT and WIN, respectively. Conversely, as more vegetation leads to lower outdoor temperatures, heating energy demands are slightly higher than in the base case. Accordingly, *MS-AllVeg* causes increases in heating energy demands by 1.0% and 0.4% in AUT and WIN, respectively. In *MS-HPN*, however, the tendency of increased energy demands found in SUM also persists in AUT and WIN, amounting to 0.9% and 0.8%, respectively. An explanation for that is the better insulation levels of the buildings' envelopes which lead to less *urban self-heating* and consequently slightly lower air temperatures [139].

Overall, the level of the energy demands is highest in WIN with about 13,400 kWh of heating energy for the whole building during the simulated week. In SUM, the cooling energy demand of SB1 amounts to between about 6400 kWh in *MS-AllVeg* to 8250 kWh in *MS-NoVeg*. As the temperature differences between the indoor setpoints to outdoor conditions are smallest in AUT, the total energy demand during this period is lower than in SUM and WIN, amounting to about 5200 kWh. The specific energy demands per square meter GFA [kWh m^{-2}_{GFA}] of *MS-Base* in SUM, AUT, and WIN are 1.1 kWh m^{-2}_{GFA}, 0.9 kWh m^{-2}_{GFA}, and 2.2 kWh m^{-2}_{GFA}, respectively.

When looking at the simulated energy demands per floor, large differences can be noticed (see Fig. 13). From Fig. 13a, especially the differences between the lower two floors to the upper nine are apparent in SUM. While in *MS-Base*, *MS-AllVeg*, and *MS-HPN* floors 5–13 have an energy demand between 138% and 188% higher than in the respective scenario on the first two floors, the differences are smaller within *MS-NoVeg* (58%–63%) where the energy demand is generally higher. As the lower floors (1–4) have adjacent buildings on the northwest and southeast façade, the area exposed to the ambient conditions becomes lower. Furthermore, shading levels from surrounding buildings and terrain are higher on lower floors. Especially during SUM, this can lead to significant reductions in solar heat gains and thus cooling energy demands.

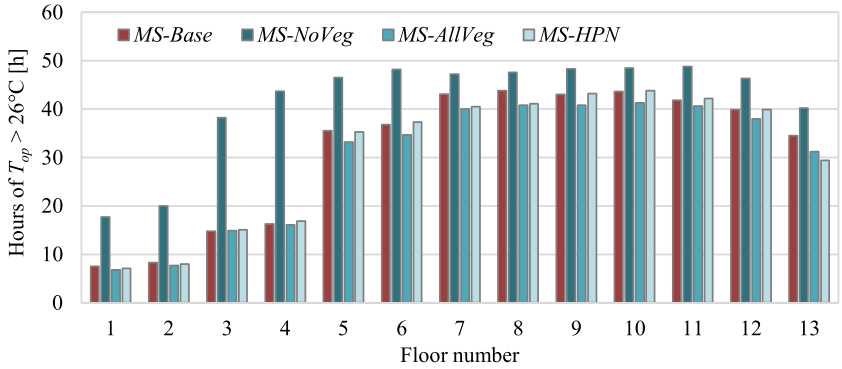

Fig. 14. Number of hours above 26 °C for the single floors during SUM, when SB1 is simulated without cooling.

The situation in AUT and WIN (Fig. 13b and c) on the other hand is very different. In AUT, the heating energy demands of floors 1–12 are fairly similar, while floor 13 shows demands about 2.4 times as high. In WIN, the differences are slightly less pronounced and the heating energy demand of all investigated scenarios on floor 13 is about 71% higher than in floors 5–12, the difference to floors 1 and 2 is ca. 104%. The main reason for this is the additional envelope area of the roof where significant amounts of energy are lost through heat transmission but also infiltration during the heating period.

Certainly, influenced by 22% less wall surface area, floors 1 and 2 show overall the best energy performance throughout all seasons. In WIN, where the differences in air temperatures at SB1 between the investigated MSs were fairly small and solar heat gains are almost negligible, this difference resulted in about 20% lower heating energy demands on the 1st floor, compared to the average of floors 5–12. During AUT, however, the 4th floor shows the lowest heating energy demands, mainly because of two reasons. First, it is less shaded towards the south than its lower floors, providing higher solar heat gains. And second, because there is an adjacent building on a part of the northwestern façade, its exposed surface area to ambient conditions is effectively reduced. In SUM, on the other hand, where the differences in microclimatic conditions between the investigated MSs are significant, the distribution of energy demand among the floors cannot be solely explained by a lower external wall surface of the lower floors. There, the cooling energy is primarily dependent on the microclimatic conditions which showed the largest differences near the ground level.

When simulating SB1 in SUM without an active cooling system, the investigated scenarios can be compared in terms of $N_{T_{op}>26\ °C}$ (see Fig. 14), a threshold that is regulated in the Norwegian building code [138]. Similar to the distribution of cooling energy demands, the lowest floors also have the lowest $N_{T_{op}>26\ °C}$. Across all floors and scenarios, values range from 6.8 h on the first floor in *MS-AllVeg*, to 48.8 h on floor 11 in *MS-NoVeg*. While the differences among the investigated scenarios are rather small from floors 5–13 (from 17% to 40% between the highest and lowest value on each floor), especially on the first four floors, *MS-NoVeg* exceeds *MS-AllVeg* by 160%–171%. Floor 13 benefits from the additional envelope area from the roof to cool down during the night which also has a positive effect on the floor below. On both floors, the thermal inertia of the building delays re-exceeding 26 °C during the day when they were effectively cooled down the night before. The mean values of $N_{T_{op}>26\ °C}$ across all floors are 31.5 h, 41.6 h, 29.7 h, and 30.8 h for *MS-Base*, *MS-NoVeg*, *MS-AllVeg*, and *MS-HPN*, respectively.

6. Discussion

6.1. Interpretation of results

The presented results show a distinct effect of the urban surface on urban microclimatic conditions and consequently on building energy demands. This effect, however, is inherently linked to the seasonal cycle of meteorological conditions. Especially in the polar and subpolar regions, the shift in meteorological conditions over the year is most significant particularly with regard to the sun, the most dominant source of energy on the Earth's surface. As a consequence, this study showed that the impact of different material compositions of the urban surface on the microclimate is fairly small in winter, even with large-scale modifications like in *MS-NoVeg* or *MS-AllVeg*. The resulting differences in heating energy demand between *MS-Base* and the other three investigated MSs during the simulated week in December were in the range of −0.5% to +0.8%. After all, the main difference between concrete and earth with grass as surface materials is the evapotranspiration ability of grass depending on the amount of solar irradiance.

In summer on the other hand, close to the ground surface, the largest differences between the investigated microclimate scenarios occurred. While *MS-AllVeg* only slightly reduces the summerly cooling demands and $N_{T_{op}>26\ °C}$, it must be remembered that the city of Trondheim has considerable amounts of green spaces already in the base case scenario. Moreover, the NTNU campus with the investigated building SB1 is surrounded by a green belt with numerous trees and expansive green areas. Rather than the difference to the base case, the differences between scenarios *MS-NoVeg* and *MS-AllVeg* should be considered. During heat waves such as in SUM in this study, proximity to green spaces which provide significant amounts of evapotranspiration proved to be an effective means to reduce the energy demand for cooling or improve indoor thermal comfort when no cooling system is available. On the 1st floor, an urban surface made of concrete instead of grass doubled cooling energy demands and increased $N_{T_{op}>26\ °C}$ by 160%. It must be kept in mind that the BPS results in this study are obtained from simulating an office building where internal heat loads are generally rather high. However, the microclimatic conditions resulting from the investigated MSs in the CFD simulations are equally marked and valid

for any type of building. Considering the negative impacts on health from cold and heat stress that have been reported even in Scandinavia [18,19,140], accommodations for vulnerable population groups should be preferably on the lower floors of buildings surrounded by expansive green areas. As shown, heat waves will be mitigated while the thermal effects in autumn and winter are relatively small. Nevertheless, especially in the transitional seasons, access to solar radiation can effectively reduce heating demands as unobstructed, south-oriented windows can be net-energy gainers throughout the year [141,142]. At the same time, ensuring solar access on the lower floors of a building in a dense neighborhood in Scandinavia is often challenging outside of the summer months.

Arguably, because summers in Trondheim are relatively short and mild, the investigated week in June 2020 cannot be regarded as typical, nor representative for the season. On the other hand, the investigated summer conditions are more common in South Norway. As global temperatures are rising, also Scandinavia will experience periods of extensive heat more and more frequently in the future [143]. Unlike in countries with warmer climates, neither the people nor buildings are adequately prepared for such a development. It is a known problem that well-insulated office buildings suffer from increased cooling demands because heat from internal sources gets trapped inside [80,144]. However, it needs to be kept in mind that only very few buildings in Norway are equipped with cooling systems. Furthermore, opening the windows for natural ventilation purposes is often not an option due to noise from the outside, air pollution from nearby roads, allergies, etc. The generally well-insulated building stock in the Nordic countries is therefore particularly susceptible to overheating. Additionally, it needs to be kept in mind that the simulations in this study were carried out for a rather poorly insulated building. For well-insulated and airtight buildings, even higher cooling energy demands and a more distinct increase of $N_{T_{op}>26\,^{\circ}C}$ can be expected. At the same time, well-insulated buildings will generally have less benefit from slightly higher outdoor temperatures during the heating season [145]. In other words, the heating energy savings potential for modern, well-insulated, and airtight buildings during the heating season due to slightly warmer microclimatic conditions can be reasonably expected to be even smaller than reported in this study.

An aspect often overlooked is the benefit of greening on mental health and the reduction of stress which has been reported in many studies [146–148]. Particularly in Japan, the concept of *shinrin-yoku* which might be translated as *taking in the forest atmosphere or forest bathing* is a well and long-known method for stress-reduction and relaxation [149,150]. Even from within buildings, briefly viewing natural features like green spaces, trees, birds, etc. through the windows allow people opportunities for so-called *micro-restorative* experiences [151].

Just as important to consider is urban stormwater management. The steadily progressing sealing of the urban surface puts increasing pressure on the public sewage systems as water runoff increases [152,153]. In Norway, not only temperatures are expected to rise due to climate change, but also precipitation levels by about 18% [154]. Several studies underlined the efficacy of urban green areas to reduce peak runoff levels in urban environments [155,156]. Even the trees themselves contribute to stormwater retention by temporarily withholding a portion of the rainfall in the crowns and directing it down the trunk into the soil and their root network [157,158].

Regarding the investigated *MS-HPN* scenario, improving the envelope insulation properties of the explicitly modeled buildings surrounding SB1 had a noticeable effect both on the air temperature at SB1 and its energy demands. Considering that only a very small fraction of all buildings in Trondheim's urbanized area were taken into account here, the effects of a city-wide building envelope upgrade are expected to be even more apparent. To ensure comparability with the other scenarios, the building envelope of the building of interest was not modified in *MS-HPN*.

6.2. Limitations

The simulations and results presented in this study are subject to several limitations that are important to have in mind. The limitations connected to the CFD simulations in this study are reported in detail in a previous study [113]. There, a detailed validation process of the CFD model was presented and it can be reasonably assumed that the microclimatic conditions in the present work are predicted with similar accuracy.

Some limitations also apply to the BPS. First of all, only one zone per floor was modeled. Mainly, this decision was governed by the way the Norwegian standards for the dynamic assessment of indoor climate and energy demand using BPS are defined. The loads and occupancy schedules in the standards might not be realistic in the case of the investigated building, however, no measured data from SB1 was available to be used instead. On the other hand, for the present comparative study, this simplification is not considered to be critical.

Furthermore, the windows were modeled in a way so that they are not opened for natural ventilation because the Norwegian standards do not contain guidelines for it. In reality, opening windows is an easy and fast measure to deal with overheating in buildings. Also, it is questionable how representative the deployed automatic control for the window blinds is. In reality, the blinds are drawn manually and do not follow a rule-based strategy. However, such user behavior is difficult to model and it was not regarded as critical for the purpose of this study.

Lastly, the pressure coefficients were determined as an average value per building façade. As was shown in Fig. 9, the distribution of pressure coefficients across a façade is very heterogeneous. Subdividing the single façades into several smaller surfaces would better represent the pressure conditions on the building envelope but also require considerably more modeling work. However, as it is the standard procedure in BPS, it was deemed sufficient not to depart from common practice and façade-averaged pressure coefficients were used in this study.

Finally, there are two general limitations to this study. First, only three one-week periods were simulated which limits the extent to which the actual influence of different urban surface compositions on the microclimate and building energy demands can be estimated over an entire year. Certainly, a whole-year simulation using representative climate data as meteorological input would deliver more conclusive results. But considering the computational expense necessary for annual, dynamic CFD simulations made such an approach

in the context of this study unfeasible.

Second, this study pursued a one-way coupling approach of type B. Consequently, no BPS results were fed back to CFD for an iteratively updated solution using more precise input data on the heat fluxes through the building envelope of the investigated building. Again, implementing such a coupling mechanism and interface between the two simulation tools would have required extensive additional modeling work which was not realizable in the context of this study.

7. Conclusion

In this study, unsteady Reynolds-averaged Navier-Stokes CFD simulations with a validated model of the urban area around the NTNU campus in Trondheim, Norway, were carried out for four different compositions of the urban surface and in three different seasons. The specific microclimatic conditions around an office high-rise building at the NTNU campus were extracted from these simulations and used for BPS of the building of interest. The exported variables were air temperature, wind speed, and wind direction. Moreover, façade-averaged pressure coefficients were determined from the CFD simulations and used in BPS.

In summary, the presented results are evidence of the benefits from vast urban greening in Norwegian, coastal climate conditions during a summerly heat wave. A concrete-sealed urban surface led to 28.5% higher cooling energy demands compared to an entirely greened urban surface. Especially at the lower floors, the positive effect of evapotranspiration from grass surfaces and trees was noticeable, leading for instance to 51% savings in cooling energy demand on the 1st floor. The savings potential decreases with increasing floor number but still amounts to 9% on the 13th floor. During the simulated weeks in autumn and winter, on the other hand, an urban surface entirely composed of concrete surfaces resulted in 3.5% and 0.9% lower energy demands for heating in the investigated building compared to intense urban greening. Considering the long winters in Trondheim and probably most of Scandinavia, a few percent of heating energy reduction are expected to add up to higher total energy savings over the year, than high reductions in cooling energy demand during relatively short heat waves.

It was also found that improving the envelope insulation properties of the explicitly modeled buildings surrounding SB1 in the CFD simulations had a noticeable effect both on the air temperature at SB1 and its energy demands in BPS. The simulated energy demands were higher than in the base case scenario by 0.8%, 0.9%, and 0.8% for summer, autumn, and winter, respectively.

The present study underlines the importance of a multi-perspective and interdisciplinary approach in city planning and emphasizes the benefits of urban green for both the built environment and urban dwellers. One-dimensional approaches to create future city districts or redevelop existing neighborhoods do not meet the complex requirements that people inherently pose to an urban environment. The CFD-BPS coupling approach presented in this work only touches upon this complexity by highlighting the far-reaching interactions between the urban fabric, urban microclimate, and building energy demand.

This study demonstrates that the common approach in BPS to use weather data from far-away airports does not consider the extremely important effects of the local urban surface on the location-specific climate data. Particularly considering the vast and open concrete surfaces at an airport, the validity of using such weather files must be fundamentally questioned if used in entirely different settings. However, high-quality and statistically representative annual weather datasets including all relevant climate variables are rarely available for the exact location of interest, and the common time and financial budgets in ordinary building projects do not allow for applying a CFD-BPS coupling strategy as presented in this study due to its complexity. While it might not be realistic that this approach will be used in general practice soon, it is extremely important to spread knowledge about local climatic effects on the building energy performance and equally important both indoor and outdoor thermal comfort for urban dwellers. Furthermore, studies like the present are important for understanding observed effects and developing new, simpler, and quicker analysis methods. Future studies should consider longer simulation periods, improved coupling strategies, and above all implement water vapor transfer and snow-covered surfaces into the CFD simulations where the climatic circumstances of the investigated location demand it. Furthermore, quantifying the difference obtained from using the CFD-BPS coupling approach compared to a pure BPS study where local climate data at the building of interest are obtained from high-quality and high-resolution measurements could be addressed in a future study.

CRediT authorship contribution statement

J. Brozovsky: Conceptualization, Methodology, Software, Formal analysis, Investigation, Visualization, Writing – original draft, Writing – review & editing, Project administration. **J. Radivojevic:** Software, Formal analysis, Writing – review & editing. **A. Simonsen:** Software, Writing – review & editing.

Declaration of competing interest

The authors declare that they have no known competing financial interests or personal relationships that could have appeared to influence the work reported in this paper.

Acknowledgments

This paper has been written within the Research Centre on Zero Emission Neighbourhoods in Smart Cities (FME ZEN). The authors gratefully acknowledge the support from the ZEN partners and the Research Council of Norway. The simulations were performed on resources provided by UNINETT Sigma2 - the National Infrastructure for High Performance Computing and Data Storage in Norway. The sea surface temperature data of the Sentinel-3 Sea and Land Surface Temperature Radiometer was provided by EUMETSAT in the Sentinel-3 Marine Copernicus Online Data Access (CODA) Web Service (https://coda.eumetsat.int/). Images from ANSYS Fluent used courtesy of ANSYS, Inc. The first author of this paper gratefully acknowledges the valuable discussions with Christoph Nickl and the

useful inputs he provided.

References

[1] O. Edenhofer (Ed.), Climate Change 2014: Mitigation of Climate Change Working Group III Contribution to the Fifth Assessment Report of the Intergovernmental Panel on Climate Change, Cambridge University Press, New York (USA), 2014.
[2] United Nations, Department of Economic and Social Affairs, Population Division, World Urbanization Prospects: the 2018 Revision, Online Edition, New York, USA, 2018.
[3] United Nations, Transforming Our World, The 2030 Agenda, For Sustainable Development, 2015.
[4] D. Barriopedro, E.M. Fischer, J. Luterbacher, R.M. Trigo, R. Garcia-Herrera, The hot summer of 2010: redrawing the temperature record map of europe, Science 332 (2011) 220–224, https://doi.org/10.1126/science.1201045.
[5] G.A. Meehl, C. Tebaldi, More intense, more frequent, and longer lasting heat waves in the 21st century, Science 305 (2004) 994–997, https://doi.org/10.1126/science.1098704.
[6] S.E. Perkins-Kirkpatrick, P.B. Gibson, Changes in regional heatwave characteristics as a function of increasing global temperature, Sci. Rep. 7 (2017) 12256, https://doi.org/10.1038/s41598-017-12520-2.
[7] T.R. Oke, G. Mills, A. Christen, J.A. Voogt, Urban Climates, Cambridge University Press, Cambridge, 2017.
[8] G.J. Steeneveld, S. Koopmans, B.G. Heusinkveld, L.W.A. van Hove, A.A.M. Holtslag, Quantifying urban heat island effects and human comfort for cities of variable size and urban morphology in The Netherlands, J. Geophys. Res. 116 (2011) 94, https://doi.org/10.1029/2011JD015988.
[9] R. Watkins, J. Palmer, M. Kolokotroni, Increased temperature and intensification of the urban heat island: implications for human comfort and urban design, Built. Environ. 33 (2007) 85–96, https://doi.org/10.2148/benv.33.1.85.
[10] A. Urban, H. Davídkovová, J. Kyselý, Heat- and cold-stress effects on cardiovascular mortality and morbidity among urban and rural populations in the Czech Republic, Int. J. Biometeorol. 58 (2014) 1057–1068, https://doi.org/10.1007/s00484-013-0693-4.
[11] D. D'Ippoliti, P. Michelozzi, C. Marino, F. de'Donato, B. Menne, K. Katsouyanni, U. Kirchmayer, A. Analitis, M. Medina-Ramón, A. Paldy, R. Atkinson, S. Kovats, L. Bisanti, A. Schneider, A. Lefranc, C. Iñiguez, C.A. Perucci, The impact of heat waves on mortality in 9 European cities: results from the EuroHEAT project, Environ. Health 9 (2010) 37, https://doi.org/10.1186/1476-069X-9-37.
[12] M. Davies, P. Steadman, T. Oreszczyn, Strategies for the modification of the urban climate and the consequent impact on building energy use, Energy Pol. 36 (2008) 4548–4551, https://doi.org/10.1016/j.enpol.2008.09.013.
[13] M. Kolokotroni, I. Giannitsaris, R. Watkins, The effect of the London urban heat island on building summer cooling demand and night ventilation strategies, Sol. Energy 80 (2006) 383–392, https://doi.org/10.1016/j.solener.2005.03.010.
[14] E. Vardoulakis, D. Karamanis, A. Fotiadi, G. Mihalakakou, The urban heat island effect in a small Mediterranean city of high summer temperatures and cooling energy demands, Sol. Energy 94 (2013) 128–144, https://doi.org/10.1016/j.solener.2013.04.016.
[15] J. Brozovsky, N. Gaitani, A. Gustavsen, A systematic review of urban microclimate in cold and polar climate regions, Renew. Sustain. Energy Rev. 138 (2021), 110551, https://doi.org/10.1016/j.rser.2020.110551.
[16] V. Miles, I. Esau, Surface urban heat islands in 57 cities across different climates in northern Fennoscandia, Urban Clim. 31 (2020), 100575, https://doi.org/10.1016/j.uclim.2019.100575.
[17] I. Esau, V. Miles, A. Soromotin, O. Sizov, M. Varentsov, P. Konstantinov, Urban heat islands in the Arctic cities: an updated compilation of in situ and remote-sensing estimations, Adv. Sci. Res. 18 (2021) 51–57, https://doi.org/10.5194/asr-18-51-2021.
[18] Z.S. Venter, N.H. Krog, D.N. Barton, Linking green infrastructure to urban heat and human health risk mitigation in Oslo, Norway, Sci. Total Environ. 709 (2020) 136193, https://doi.org/10.1016/j.scitotenv.2019.136193.
[19] D. Oudin Åström, C. Åström, B. Forsberg, A.M. Vicedo-Cabrera, A. Gasparrini, A. Oudin, K. Sundquist, Heat wave-related mortality in Sweden: a case-crossover study investigating effect modification by neighbourhood deprivation, Scand. J. Publ. Health 48 (2020) 428–435, https://doi.org/10.1177/1403494818801615.
[20] IEA - International Energy Agency, The Future of Cooling, 2018.
[21] S.A. Lowe, An energy and mortality impact assessment of the urban heat island in the US, Environ. Impact Assess. Rev. 56 (2016) 139–144, https://doi.org/10.1016/j.eiar.2015.10.004.
[22] J. Yang, E. Bou-Zeid, Should cities embrace their heat islands as shields from extreme cold? J. Appl. Meteorol. Climatol. 57 (2018) 1309–1320, https://doi.org/10.1175/JAMC-D-17-0265.1.
[23] V.V. Klimenko, A.S. Ginzburg, P.F. Demchenko, A.G. Tereshin, I.N. Belova, E.V. Kasilova, Impact of urbanization and climate warming on energy consumption in large cities, Dokl. Phys. 61 (2016) 521–525, https://doi.org/10.1134/S1028335816100050.
[24] F. Meng, J. Guo, G. Ren, L. Zhang, R. Zhang, Impact of urban heat island on the variation of heating loads in residential and office buildings in Tianjin, Energy Build. 226 (2020), 110357, https://doi.org/10.1016/j.enbuild.2020.110357.
[25] F. Ding, H. Pang, W. Guo, Impact of the urban heat island on residents' energy consumption: a case study of Qingdao, IOP Conf. Ser. Earth Environ. Sci. 121 (2018), 32026, https://doi.org/10.1088/1755-1315/121/3/032026.
[26] A. Mohajerani, J. Bakaric, T. Jeffrey-Bailey, The urban heat island effect, its causes, and mitigation, with reference to the thermal properties of asphalt concrete, J. Environ. Manag. 197 (2017) 522–538, https://doi.org/10.1016/j.jenvman.2017.03.095.
[27] T.R. Oke, The energetic basis of the urban heat island, Q. J. Roy. Meteorol. Soc. 108 (1982) 1–24, https://doi.org/10.1002/qj.49710845502.
[28] G. Mills, Urban climatology: history, status and prospects, Urban Clim. 10 (2014) 479–489, https://doi.org/10.1016/j.uclim.2014.06.004.
[29] Y. Toparlar, B. Blocken, B. Maiheu, G. van Heijst, A review on the CFD analysis of urban microclimate, Renew. Sustain. Energy Rev. 80 (2017) 1613–1640, https://doi.org/10.1016/j.rser.2017.05.248.
[30] P.A. Mirzaei, F. Haghighat, Approaches to study urban heat island – abilities and limitations, Build. Environ. 45 (2010) 2192–2201, https://doi.org/10.1016/j.buildenv.2010.04.001.
[31] I. Orlanski, A rational subdivision of scales for atmospheric processes, Bull. Am. Meteorol. Soc. 56 (1975) 527–530.
[32] B. Blocken, W.D. Janssen, T. van Hooff, CFD simulation for pedestrian wind comfort and wind safety in urban areas: general decision framework and case study for the Eindhoven University campus, Environ. Model. Software 30 (2012) 15–34, https://doi.org/10.1016/j.envsoft.2011.11.009.
[33] B. Blocken, J. Persoon, Pedestrian wind comfort around a large football stadium in an urban environment: CFD simulation, validation and application of the new Dutch wind nuisance standard, J. Wind Eng. Ind. Aerod. 97 (2009) 255–270, https://doi.org/10.1016/j.jweia.2009.06.007.
[34] B. Blocken, S. Roels, J. Carmeliet, Modification of pedestrian wind comfort in the Silvertop Tower passages by an automatic control system, J. Wind Eng. Ind. Aerod. 92 (2004) 849–873, https://doi.org/10.1016/j.jweia.2004.04.004.
[35] W.D. Janssen, B. Blocken, T. van Hooff, Pedestrian wind comfort around buildings: comparison of wind comfort criteria based on whole-flow field data for a complex case study, Build. Environ. 59 (2013) 547–562, https://doi.org/10.1016/j.buildenv.2012.10.012.
[36] M.S. Fadl, J. Karadelis, CFD simulation for wind comfort and safety in urban area: a case study of coventry university central campus, Int. J. Archit. Eng. Constr. 2 (2013) 131–143, https://doi.org/10.7492/IJAEC.2013.013.
[37] C. Gromke, B. Blocken, Influence of avenue-trees on air quality at the urban neighborhood scale. Part I: quality assurance studies and turbulent Schmidt number analysis for RANS CFD simulations, Environ. Pollut. 196 (2015) 214–223, https://doi.org/10.1016/j.envpol.2014.10.016.
[38] C. Gromke, B. Blocken, Influence of avenue-trees on air quality at the urban neighborhood scale. Part II: traffic pollutant concentrations at pedestrian level, Environ. Pollut. 196 (2015) 176–184, https://doi.org/10.1016/j.envpol.2014.10.015.
[39] J.H. Amorim, V. Rodrigues, R. Tavares, J. Valente, C. Borrego, CFD modelling of the aerodynamic effect of trees on urban air pollution dispersion, Sci. Total Environ. 461–462 (2013) 541–551, https://doi.org/10.1016/j.scitotenv.2013.05.031.

[40] P. Gousseau, B. Blocken, T. Stathopoulos, G. van Heijst, CFD simulation of near-field pollutant dispersion on a high-resolution grid: a case study by LES and RANS for a building group in downtown Montreal, Atmos. Environ 45 (2011) 428–438, https://doi.org/10.1016/j.atmosenv.2010.09.065.
[41] B. Blocken, J. Carmeliet, The influence of the wind-blocking effect by a building on its wind-driven rain exposure, J. Wind Eng. Ind. Aerod. 94 (2006) 101–127, https://doi.org/10.1016/j.jweia.2005.11.001.
[42] B. Blocken, J. Carmeliet, Validation of CFD simulations of wind-driven rain on a low-rise building facade, Build. Environ. 42 (2007) 2530–2548, https://doi.org/10.1016/j.buildenv.2006.07.032.
[43] T. van Hooff, B. Blocken, M. van Harten, 3D CFD simulations of wind flow and wind-driven rain shelter in sports stadia: influence of stadium geometry, Build. Environ. 46 (2011) 22–37, https://doi.org/10.1016/j.buildenv.2010.06.013.
[44] A. Ghaffarianhoseini, U. Berardi, A. Ghaffarianhoseini, K. Al-Obaidi, Analyzing the thermal comfort conditions of outdoor spaces in a university campus in Kuala Lumpur, Malaysia, Sci. Total Environ. 666 (2019) 1327–1345, https://doi.org/10.1016/j.scitotenv.2019.01.284.
[45] H. Lee, H. Mayer, L. Chen, Contribution of trees and grasslands to the mitigation of human heat stress in a residential district of Freiburg, Southwest Germany, Landsc. Urban Plann. 148 (2016) 37–50, https://doi.org/10.1016/j.landurbplan.2015.12.004.
[46] J. Brozovsky, S. Corio, N. Gaitani, A. Gustavsen, Evaluation of sustainable strategies and design solutions at high-latitude urban settlements to enhance outdoor thermal comfort, Energy Build. 244 (2021), 111037, https://doi.org/10.1016/j.enbuild.2021.111037.
[47] P.A. Mirzaei, CFD modeling of micro and urban climates: problems to be solved in the new decade, Sustain. Cities Soc. 69 (2021), 102839, https://doi.org/10.1016/j.scs.2021.102839.
[48] F.-K. Benra, H.J. Dohmen, J. Pei, S. Schuster, B. Wan, A comparison of one-way and two-way coupling methods for numerical analysis of fluid-structure interactions, J. Appl. Math. (2011) 1–16, https://doi.org/10.1155/2011/853560, 2011.
[49] E. Djunaedy, J. Hensen, M. Loomans, External coupling between CFD and energy simulation: implementation and validation, ASHRAE Transactions 111 (2005) 612–624.
[50] Z.J. Zhai, Q.Y. Chen, Performance of coupled building energy and CFD simulations, Energy Build. 37 (2005) 333–344, https://doi.org/10.1016/j.enbuild.2004.07.001.
[51] Q. Kong, J. Feng, C. Yang, Z. Miao, X. He, Numerical simulation of a radiant floor cooling office based on CFD-BES coupling and FEM, Energy Proc. 105 (2017) 3577–3583, https://doi.org/10.1016/j.egypro.2017.03.825.
[52] M. Barbason, S. Reiter, Coupling building energy simulation and computational fluid dynamics: application to a two-storey house in a temperate climate, Build. Environ. 75 (2014) 30–39, https://doi.org/10.1016/j.buildenv.2014.01.012.
[53] Y. Fan, K. Ito, Optimization of indoor environmental quality and ventilation load in office space by multilevel coupling of building energy simulation and computational fluid dynamics, Build. Simulat. 7 (2014) 649–659, https://doi.org/10.1007/s12273-014-0178-3.
[54] W. Tian, X. Han, W. Zuo, M.D. Sohn, Building energy simulation coupled with CFD for indoor environment: a critical review and recent applications, Energy Build. 165 (2018) 184–199, https://doi.org/10.1016/j.enbuild.2018.01.046.
[55] X. Shan, N. Luo, K. Sun, T. Hong, Y.-K. Lee, W.-Z. Lu, Coupling CFD and building energy modelling to optimize the operation of a large open office space for occupant comfort, Sustain. Cities Soc. 60 (2020), 102257, https://doi.org/10.1016/j.scs.2020.102257.
[56] S. Gracik, M. Heidarinejad, J. Liu, J. Srebric, Effect of urban neighborhoods on the performance of building cooling systems, Build. Environ. 90 (2015) 15–29, https://doi.org/10.1016/j.buildenv.2015.02.037.
[57] M. Hadavi, H. Pasdarshahri, Investigating effects of urban configuration and density on urban climate and building systems energy consumption, J. Build. Eng. (2021), https://doi.org/10.1016/j.jobe.2021.102710.
[58] U.S. Department of Energy, EnergyPlus Version 9.5.0 Documentation: Engineering Reference, 2021.
[59] G.M. Stavrakakis, D.A. Katsaprakakis, M. Damasiotis, Basic principles, most common computational tools, and capabilities for building energy and urban microclimate simulations, Energies 14 (2021) 6707, https://doi.org/10.3390/en14206707.
[60] J. Bouyer, C. Inard, M. Musy, Microclimatic coupling as a solution to improve building energy simulation in an urban context, Energy Build. 43 (2011) 1549–1559, https://doi.org/10.1016/j.enbuild.2011.02.010.
[61] L. Malys, M. Musy, C. Inard, Microclimate and building energy consumption: study of different coupling methods, Adv. Build. Energy Res. 9 (2015) 151–174, https://doi.org/10.1080/17512549.2015.1043643.
[62] A. Gros, E. Bozonnet, C. Inard, M. Musy, Simulation Tools to Assess Microclimate and Building Energy – A Case Study on the Design of a New District, Energy Build, vol. 114, 2016, pp. 112–122, https://doi.org/10.1016/j.enbuild.2015.06.032.
[63] B. Morille, M. Musy, L. Malys, Preliminary study of the impact of urban greenery types on energy consumption of building at a district scale: academic study on a canyon street in Nantes (France) weather conditions, Energy Build. 114 (2016) 275–282, https://doi.org/10.1016/j.enbuild.2015.06.030.
[64] L. Merlier, L. Frayssinet, F. Kuznik, G. Rusaouën, K. Johannes, J.-L. Hubert, M. Milliez, Analysis of the (Urban) Microclimate Effects on the Building Energy Behaviour, Proc. 15th Int. Build. Perform. Simul. Assoc. Conf., San Francisco, CA, USA), 2017.
[65] R. Zhang, P.A. Mirzaei, B. Jones, Development of a dynamic external CFD and BES coupling framework for application of urban neighbourhoods energy modelling, Build. Environ. 146 (2018) 37–49, https://doi.org/10.1016/j.buildenv.2018.09.006.
[66] R. Zhang, P.A. Mirzaei, Fast and dynamic urban neighbourhood energy simulation using CFDf-CFDc-BES coupling method, Sustain. Cities Soc. 66 (2021), 102545, https://doi.org/10.1016/j.scs.2020.102545.
[67] R. Zhang, P.A. Mirzaei, Virtual dynamic coupling of computational fluid dynamics-building energy simulation-artificial intelligence: case study of urban neighbourhood effect on buildings' energy demand, Build. Environ. 195 (2021), 107728, https://doi.org/10.1016/j.buildenv.2021.107728.
[68] X. Yang, L. Zhao, M. Bruse, Q. Meng, An integrated simulation method for building energy performance assessment in urban environments, Energy Build. 54 (2012) 243–251, https://doi.org/10.1016/j.enbuild.2012.07.042.
[69] Y.K. Yi, N. Feng, Dynamic integration between building energy simulation (BES) and computational fluid dynamics (CFD) simulation for building exterior surface, Build. Simulat. 6 (2013) 297–308, https://doi.org/10.1007/s12273-013-0116-9.
[70] J. Liu, M. Heidarinejad, M. Guo, J. Srebric, Numerical evaluation of the local weather data impacts on cooling energy use of buildings in an urban area, Procedia Eng. 121 (2015) 381–388, https://doi.org/10.1016/j.proeng.2015.08.1082.
[71] C.P. Skelhorn, G. Levermore, S.J. Lindley, Impacts on cooling energy consumption due to the UHI and vegetation changes in Manchester, UK, Energy Build. 122 (2016) 150–159, https://doi.org/10.1016/j.enbuild.2016.01.035.
[72] K. Gobakis, D. Kolokotsa, Coupling building energy simulation software with microclimatic simulation for the evaluation of the impact of urban outdoor conditions on the energy consumption and indoor environmental quality, Energy Build. 157 (2017) 101–115, https://doi.org/10.1016/j.enbuild.2017.02.020.
[73] K.-T. Huang, Y.-J. Li, Impact of street canyon typology on building's peak cooling energy demand: a parametric analysis using orthogonal experiment, Energy Build. 154 (2017) 448–464, https://doi.org/10.1016/j.enbuild.2017.08.054.
[74] K. Javanroodi, V.M. Nik, Impacts of microclimate conditions on the energy performance of buildings in urban areas, Buildings 9 (2019) 189, https://doi.org/10.3390/buildings9080189.
[75] J. Liu, M. Heidarinejad, S.K. Nikkho, N.W. Mattise, J. Srebric, Quantifying impacts of urban microclimate on a building energy consumption—a case study, Sustainability 11 (2019) 4921, https://doi.org/10.3390/su11184921.
[76] J. Natanian, D. Maiullari, A. Yezioro, T. Auer, Synergetic urban microclimate and energy simulation parametric workflow, J. Phys.: Conf. Ser. 1343 (2019), 12006, https://doi.org/10.1088/1742-6596/1343/1/012006.
[77] M. Shirzadi, M. Naghashzadegan, P.A. Mirzaei, Developing a framework for improvement of building thermal performance modeling under urban microclimate interactions, Sustain. Cities Soc. 44 (2019) 27–39, https://doi.org/10.1016/j.scs.2018.09.016.
[78] M. Mosteiro-Romero, D. Maiullari, M. Pijpers-van Esch, A. Schlueter, An integrated microclimate-energy demand simulation method for the assessment of urban districts, Front. Built Environ. 6 (2020) 94, https://doi.org/10.3389/fbuil.2020.553946.
[79] P. Shen, Z. Wang, How neighborhood form influences building energy use in winter design condition: case study of Chicago using CFD coupled simulation, J. Clean. Prod. 261 (2020), 121094, https://doi.org/10.1016/j.jclepro.2020.121094.

[80] Y. Toparlar, B. Blocken, B. Maiheu, G. van Heijst, Impact of urban microclimate on summertime building cooling demand: a parametric analysis for Antwerp, Belgium, Appl. Energy 228 (2018) 852–872, https://doi.org/10.1016/j.apenergy.2018.06.110.

[81] J. Allegrini, J. Kämpf, V. Dorer, J. Carmeliet, Modelling the urban microclimate and its influence on building energy demands of an urban neighbourhood, Proceedings of CISBAT II (2013) 867–872. International Conference Cleantech for Smart Cities & Buildings from Nano to Urban Scale in Lausanne, Switzerland, September 4-6 (2013.

[82] J. Allegrini, V. Dorer, J. Carmeliet, Coupled CFD, radiation and building energy model for studying heat fluxes in an urban environment with generic building configurations, Sustain. Cities Soc. 19 (2015) 385–394, https://doi.org/10.1016/j.scs.2015.07.009.

[83] J. Allegrini, V. Dorer, J. Carmeliet, Influence of morphologies on the microclimate in urban neighbourhoods, J. Wind Eng. Ind. Aerod. 144 (2015) 108–117, https://doi.org/10.1016/j.jweia.2015.03.024.

[84] J. Allegrini, J. Carmeliet, Coupled CFD and building energy simulations for studying the impacts of building height topology and buoyancy on local urban microclimates, Urban Clim. 21 (2017) 278–305, https://doi.org/10.1016/j.uclim.2017.07.005.

[85] J. Allegrini, J. Carmeliet, Simulations of local heat islands in Zürich with coupled CFD and building energy models, Urban Clim. 24 (2018) 340–359, https://doi.org/10.1016/j.uclim.2017.02.003.

[86] M. Hadavi, H. Pasdarshahri, Impacts of urban buildings on microclimate and cooling systems efficiency: coupled CFD and BES simulations, Sustain. Cities Soc. 67 (2021), 102740, https://doi.org/10.1016/j.scs.2021.102740.

[87] N.H. Wong, Y. He, N.S. Nguyen, S.V. Raghavan, M. Martin, D.J.C. Hii, Z. Yu, J. Deng, An integrated multiscale urban microclimate model for the urban thermal environment, Urban Clim. 35 (2021), 100730, https://doi.org/10.1016/j.uclim.2020.100730.

[88] G. Chen, L. Rong, G. Zhang, Comparison of urban airflow between solar-induced thermal wall and uniform wall temperature boundary conditions by coupling CitySim and CFD, Build. Environ. 172 (2020), 106732, https://doi.org/10.1016/j.buildenv.2020.106732.

[89] R. Aghamolaei, M. Fallahpour, P.A. Mirzaei, Tempo-spatial thermal comfort analysis of urban heat island with coupling of CFD and building energy simulation, Energy Build. 251 (2021), 111317, https://doi.org/10.1016/j.enbuild.2021.111317.

[90] Statistisk sentralbyrå, Kommunefakta Trondheim, 2021. https://www.ssb.no/kommunefakta/trondheim.

[91] I.D. Stewart, T.R. Oke, Local climate zones for urban temperature studies, Bull. Am. Meteorol. Soc. 93 (2012) 1879–1900, https://doi.org/10.1175/BAMS-D-11-00019.1.

[92] M.C. Peel, B.L. Finlayson, T.A. McMahon, Updated world map of the Köppen-Geiger climate classification, Hydrol. Earth Syst. Sci. Discuss. 4 (2007) 439–473, https://doi.org/10.5194/hessd-4-439-2007.

[93] E. Lundstad, O.E. Tveito, Homogenization of Daily Mean Temperature in Norway, 2016.

[94] Meteorologisk Institutt, eKlima [meanwhile shut down]: Free access to weather- and climate data from Norwegian Meteorological Institute from historical data to real time observations. Normals. http://sharki.oslo.dnmi.no/portal/page?_pageid=73,39035,73_39049&_dad=portal&_schema=PORTAL. (Accessed 11 March 2021).

[95] J.B. Palter, The role of the Gulf Stream in European climate, Ann. Rev. Mar. Sci 7 (2015) 113–137, https://doi.org/10.1146/annurev-marine-010814-015656.

[96] N. Antoniou, H. Montazeri, M. Neophytou, B. Blocken, CFD simulation of urban microclimate: validation using high-resolution field measurements, Sci. Total Environ. 695 (2019) 133743, https://doi.org/10.1016/j.scitotenv.2019.133743.

[97] Y. Toparlar, B. Blocken, P.E.J. Vos, G. van Heijst, W.D. Janssen, T. van Hooff, H. Montazeri, H. Timmermans, CFD simulation and validation of urban microclimate: a case study for Bergpolder Zuid, Rotterdam, Build. Environ 83 (2015) 79–90, https://doi.org/10.1016/j.buildenv.2014.08.004.

[98] A. Bring, P. Sahlin, M. Vuolle, Models for Building Indoor Climate and Energy Simulation: A Report of IEA SHC Task 22: Building Energy Analysis Tools, Subtask B: Model Documentation, 1999.

[99] N. Björsell, A. Bring, L. Eriksson, P. Grozman, M. Lindgren, P. Sahlin, A. Shaovalov, M. Vuolle, IDA indoor climate and energy, in: Proc. 6th Int. Build. Perform. Simul. Assoc. Conf., 1999. Kyoto, Japan.

[100] A.B. Equa Simulation, Validation of IDA Indoor Climate and Energy 4.0 Build 4 with Respect to ANSI/ASHRAE Standard 140-2004, 2010.

[101] A.B. Equa Simulation, Equa Simulation Finland Oy, Validation of IDA Indoor Climate and Energy 4.0 with Respect to CEN Standards EN 15255-2007 and EN 15265-2007, 2010.

[102] S. Moosberger, IDA ICE CIBSE-validation: test of IDA indoor climate and energy version 4.0 according to CIBSE TM33, Issue 3 (2007).

[103] E. Catto Lucchino, A. Gelesz, K. Skeie, G. Gennaro, A. Reith, V. Serra, F. Goia, Modelling double skin façades (DSFs) in whole-building energy simulation tools: validation and inter-software comparison of a mechanically ventilated single-story DSF, Build. Environ. 199 (2021), 107906, https://doi.org/10.1016/j.buildenv.2021.107906.

[104] A. Gelesz, E. Catto Lucchino, F. Goia, V. Serra, A. Reith, Characteristics that matter in a climate façade: a sensitivity analysis with building energy simulation tools, Energy Build. 229 (2020), 110467, https://doi.org/10.1016/j.enbuild.2020.110467.

[105] E. Nilsson, P. Rohdin, Empirical validation and numerical predictions of an industrial borehole thermal energy storage system, Energies 12 (2019) 2263, https://doi.org/10.3390/en12122263.

[106] J. Clauß, S. Stinner, I. Sartori, L. Georges, Predictive rule-based control to activate the energy flexibility of Norwegian residential buildings: case of an air-source heat pump and direct electric heating, Appl. Energy 237 (2019) 500–518, https://doi.org/10.1016/j.apenergy.2018.12.074.

[107] J. Clauß, L. Georges, Model complexity of heat pump systems to investigate the building energy flexibility and guidelines for model implementation, Appl. Energy 255 (2019), 113847, https://doi.org/10.1016/j.apenergy.2019.113847.

[108] B. Blocken, J. Carmeliet, T. Stathopoulos, CFD evaluation of wind speed conditions in passages between parallel buildings—effect of wall-function roughness modifications for the atmospheric boundary layer flow, J. Wind Eng. Ind. Aerod. 95 (2007) 941–962, https://doi.org/10.1016/j.jweia.2007.01.013.

[109] B. Blocken, P. Moonen, T. Stathopoulos, J. Carmeliet, Numerical study on the existence of the venturi effect in passages between perpendicular buildings, J. Eng. Mech. 134 (2008) 1021–1028.

[110] B. Blocken, T. Stathopoulos, J. Carmeliet, Wind environmental conditions in passages between two long narrow perpendicular buildings, J. Aero. Eng. 21 (2008) 280–287, https://doi.org/10.1061/(ASCE)0893-1321(2008)21:4(280).

[111] M.W. Liddament, Air Infiltration Calculation Techniques - an Application Guide, 1986. Coventry (UK).

[112] D. Cóstola, B. Blocken, J. Hensen, Overview of pressure coefficient data in building energy simulation and airflow network programs, Build. Environ. 44 (2009) 2027–2036, https://doi.org/10.1016/j.buildenv.2009.02.006.

[113] J. Brozovsky, A. Simonsen, N. Gaitani, Validation of a CFD model for the evaluation of urban microclimate at high latitudes: a case study in Trondheim, Norway, Build. Environ 205 (2021), 108175, https://doi.org/10.1016/j.buildenv.2021.108175.

[114] J. Wieringa, Updating the Davenport roughness classification, J. Wind Eng. Ind. Aerod. 41 (1992) 357–368, https://doi.org/10.1016/0167-6105(92)90434-C.

[115] T.-H. Shih, W.W. Liou, A. Shabbir, Z. Yang, J. Zhu, A new k-ε viscosity model for high Reynolds number turbulent flows, Comput. Fluids 24 (1995) 227–238, https://doi.org/10.1016/0045-7930(94)00032-T.

[116] G.K. Ntinas, X. Shen, Y. Wang, G. Zhang, Evaluation of CFD turbulence models for simulating external airflow around varied building roof with wind tunnel experiment, Build. Simulat. 11 (2018) 115–123, https://doi.org/10.1007/s12273-017-0369-9.

[117] Y. Toparlar, B. Blocken, B. Maiheu, G.J.F. van Heijst, The effect of an urban park on the microclimate in its vicinity: a case study for Antwerp, Belgium, Int. J. Climatol. 38 (2018) e303–e322, https://doi.org/10.1002/joc.5371.

[118] ANSYS Inc, ANSYS Fluent Theory Guide: Release 2020 R1 January 2020, 2020. Canonsburg, PA.

[119] ANSYS Inc., Fluent User's Guide: Release 2020 R1 January 2020, 2020. Canonsburg, PA.

[120] J.P. van Doormaal, G.D. Raithby, Enhancements of the SIMPLE method for predicting incompressible fluid flows, Numer. Heat Tran. 7 (1984) 147–163, https://doi.org/10.1080/01495728408961817.

[121] H.L. Penman, The physical bases of irrigation control, in: Report of the 13th International Horticultural Congress, 1953, pp. 1–13.

[122] J.L. Monteith, Evaporation and environment, Symp. Soc. Exp. Biol. 19 (1965) 205–234.

[123] Food and Agriculture Organisation of the United Nations, Crop evapotranspiration: guidelines for computing crop water requirements, FAO Irrigation and drainage paper 56, 1998, http://www.fao.org/3/X0490E/x0490e00.htm#Contents. (Accessed 10 December 2020).
[124] H.G. Jones, Plants and Microclimate: A Quantitative Approach to Environmental Plant Physiology, third ed., Cambridge University Press, Cambridge, 2013.
[125] M.E. Jensen, H.R. Haise, Estimating evapotranspiration from solar radiation, in: Proceedings of the American Society of Civil Engineers, Journal of the Irrigation and Drainage Division 89, 1963, pp. 15–41.
[126] Y.J. Huang, H. Akbari, H. Taha, A. Rosenfeld, The potential of vegetation in reducing summer cooling loads in residential buildings, J. Clim. Adv. Meteorol. 26 (1987) 1103–1116, https://doi.org/10.1175/1520-0450(1987)026<1103:TPOVIR>2.0.CO;2.
[127] S.R. Green, Modelling turbulent air flow in stand of widely-spaced trees, Phoenics J 5 (1992) 294–312.
[128] J. Liu, J. Chen, T.A. Black, M.D. Novak, E-ε modelling of turbulent air flow downwind of a model forest edge, Bound-Layer Meteorol 77 (1996) 21–44.
[129] C. Sanz, A Note on K-ε Modelling of Vegetation Canopy Air-Flows, Bound-Layer Meteorol, vol. 108, 2003, pp. 191–197, https://doi.org/10.1023/A:1023066012766.
[130] M. Santamouris (Ed.), Environmental Design of Urban Buildings: an Integrated Approach, Earthscan, London, 2006.
[131] Bautabellen für Ingenieure: mit Berechnungshinweisen und Beispielen, in: A. Goris, K.-J. Schneider, A. Albert (Eds.), Werner; Wolters Kluwer, nineteenth ed., 2010. Neuwied, Köln.
[132] J. Franke, C. Hirsch, A.G. Jensen, H.W. Krüs, M. Schatzmann, P.S. Westbury, S.D. Miles, J.A. Wisse, N.G. Wright, Recommendations on the use of CFD in wind engineering, in: Proc. Int. Conf. Urban Wind Engineering and Building Aerodynamics. COST Action C14, Impact of Wind and Storm on City Life Built Environment, von Karman Institute, Sint-Genesius-Rode, Belgium, 2004. May 5-7.
[133] Y. Tominaga, A. Mochida, R. Yoshie, H. Kataoka, T. Nozu, M. Yoshikawa, T. Shirasawa, AIJ guidelines for practical applications of CFD to pedestrian wind environment around buildings, J. Wind Eng. Ind. Aerod. 96 (2008) 1749–1761, https://doi.org/10.1016/j.jweia.2008.02.058.
[134] SN-NSPEK 3031, Energy performance of buildings: calculation of energy needs and energy supply, Standard Norge 01.040 91 (2020) 91–120, 10.
[135] NS 3031, Calculation of energy performance of buildings: method and data, Standard Norge 01.040 91 (2014) 91–120, 10. (Accessed 25 October 2021).
[136] K. Skeie, Sustainable Facade Renovation, Master's thesis, 2013.
[137] V. Fabi, R.V. Andersen, S. Corgnati, B.W. Olesen, Occupants' window opening behaviour: a literature review of factors influencing occupant behaviour and models, Build. Environ. 58 (2012) 188–198, https://doi.org/10.1016/j.buildenv.2012.07.009.
[138] Norwegian Building Authority, Regulations on Technical Requirements for Construction Works, 2017.
[139] J. Yang, K.W. Tham, S.E. Lee, M. Santamouris, C. Sekhar, D.K.W. Cheong, Anthropogenic heat reduction through retrofitting strategies of campus buildings, Energy Build. 152 (2017) 813–822, https://doi.org/10.1016/j.enbuild.2016.11.051.
[140] P. Nafstad, Anders Skrondal, Espen Bjertness, Mortality and temperature in Oslo, Norway, 1990-1995, Eur. J. Epidemiol. 17 (2001) 621–627.
[141] S. Grynning, A. Gustavsen, B. Time, B.P. Jelle, Windows in the buildings of tomorrow: energy losers or energy gainers? Energy Build. 61 (2013) 185–192, https://doi.org/10.1016/j.enbuild.2013.02.029.
[142] J. Brozovsky, N. Gaitani, A. Gustavsen, Characterisation of heat losses in zero emission buildings (ZEB) in cold climate, Proc. 16th Int. Build. Perform. Simul. Assoc. Conf. (Rome, Italy) (2019) 343–350, https://doi.org/10.26868/25222708.2019.210560.
[143] H.T. Tilley Tajet, Hetebølger i Norge fra 1957 - 2019 [Heat waves in Norway from 1957 - 2019], 2020.
[144] A. Boyano, P. Hernandez, O. Wolf, Energy demands and potential savings in European office buildings: case studies based on EnergyPlus simulations, Energy Build. 65 (2013) 19–28, https://doi.org/10.1016/j.enbuild.2013.05.039.
[145] R. Wang, S. Lu, X. Zhai, W. Feng, The Energy Performance and Passive Survivability of High Thermal Insulation Buildings in Future Climate Scenarios, Build. Simul., 2021, https://doi.org/10.1007/s12273-021-0818-3.
[146] P. Grahn, U.A. Stigsdotter, Landscape planning and stress, Urban For. Urban Green. 2 (2003) 1–18, https://doi.org/10.1078/1618-8667-00019.
[147] L. O'Brien, K. Williams, A. Stewart, Urban Health and Health Inequalities and the Role of Urban Forestry in Britain: A Review, 2010.
[148] J. Barton, M. Rogerson, The importance of greenspace for mental health, Br. J. Psychiatry Int. 14 (2017) 79–81.
[149] B.J. Park, Y. Tsunetsugu, T. Kasetani, T. Kagawa, Y. Miyazaki, The physiological effects of Shinrin-yoku (taking in the forest atmosphere or forest bathing): evidence from field experiments in 24 forests across Japan, Environ. Health Prev. Med. 15 (2010) 18–26, https://doi.org/10.1007/s12199-009-0086-9.
[150] Y. Tsunetsugu, B.-J. Park, Y. Miyazaki, Trends in research related to "Shinrin-yoku" (taking in the forest atmosphere or forest bathing) in Japan, Environ. Health Prev. Med. 15 (2010) 27–37.
[151] R. Kaplan, The role of nature in the context of the workplace, Landsc. Urban Plann. 26 (1993) 193–201, https://doi.org/10.1016/0169-2046(93)90016-7.
[152] A. Galderisi, E. Treccozzi, Green strategies for flood resilient cities: the benevento case study, Proc. Environ. Sci. 37 (2017) 655–666, https://doi.org/10.1016/j.proenv.2017.03.052.
[153] A. Pistocchi, C. Calzolari, F. Malucelli, F. Ungaro, Soil sealing and flood risks in the plains of Emilia-Romagna, Italy, J. Hydrol. Reg. Stud. 4 (2015) 398–409, https://doi.org/10.1016/j.ejrh.2015.06.021.
[154] Norsk Klima Service Senter, Klima I Norge 2100 [Climate in Norway 2100], 2016.
[155] S.T. Thorolfsson, A new direction in the urban runoff and pollution management in the city of Bergen, Norway, Water Sci. Technol. 38 (1998) 123–130.
[156] T. Bai, A.L. Mayer, W.D. Shuster, G. Tian, The hydrologic role of urban green space in mitigating flooding (Luohe, China), Sustainability 10 (2018) 1–3584, https://doi.org/10.3390/su10103584.
[157] Q. Xiao, E.G. McPherson, Rainfall interception by Santa Monica's municipal urban forest, Urban Ecosyst. 6 (2002) 291–302, https://doi.org/10.1023/B:UECO.0000004828.05143.67.
[158] Q. Xiao, E.G. McPherson, S.L. Ustin, M.E. Grismer, J.R. Simpson, Winter rainfall interception by two mature open-grown trees in Davis, California, Hydrol. Process. 14 (2000) 763–784, https://doi.org/10.1002/(SICI)1099-1085(200003)14:4<763:AID-HYP971>3.0.CO;2-7.